International Journal of

Thermodynamics

Editor-in-Chief
L. Kuddusi

Honorary Editors
A. Bejan
M. J. Moran
J. Szargut
G. Tsatsaronis
A. Valero
M. R. von Spakovsky

International Centre for Applied Thermodynamics

Publishing Editor

Assoc. Prof. Dr. Abdussamet SUBASI   Assist. Prof. Mustafa Yasin GÖKASLAN

Res. Assist. Ali Murat BİNARK

Language Editor

Assoc. Prof. Dr. Abdussamet SUBASI

Journal Contacts

Editor-in-Chief

Prof. Dr. Lütfullah Kuddusi

ISTANBUL TECHNICAL UNIVERSITY

kuddusi@itu.edu.tr

+902122931300/2452

*Department of Mechanical Engineering
Istanbul Technical University
Gumussuyu, 34437 Istanbul Turkey*

CONTENTS	

Research Article

A New Mnemonic Scheme to Derive Thermodynamics Equations and Maxwell Relations Based on Butterfly Symmetry Approach

[1]R. Tariverdi (ID), [2]*A. Bahramian (ID)

[1,2] Department of Chemical Engineering, Hamedan University of Technology, P.O. Box, 65155 Hamedan, Iran.
E-mail: [2]* bahramian@hut.ac.ir

Abstract

In this study, a new mnemonic scheme is proposed for a simple closed system to derive equations in classical thermodynamics potentials that connect the state variables and Maxwell relations based on the butterfly symmetry approach. The proposed method does not have the difficulties in the arrangement and sign of parameters which were found in the geometric diagrams such as square, cub octahedron, concentric multi-circle, Venn diagram, and Natarajan's thermodynamics circles. The suggested method resolves the identical elements and Maxwell's formulas in thermodynamics and energy, enthalpy, Helmholtz and Gibbs equations by creating a matrix through the butterfly symmetry strategy. The most important feature of this method is that the differential and partial derivatives of thermodynamic parameters are formed in matrix arrays. The signs are applied only according to the butterfly symmetry, and unlike the Max Born method, there is no need to pay attention to the direction of arrows.

Keywords: Mnemonic scheme; thermodynamic relations; Maxwell relations; butterfly symmetry; simple novel method.

1. Introduction

Thermodynamics is a phenomenological science based on experimental findings and fundamental laws that describe the physicochemical properties of a system as it exchanges matter and energy or reaches equilibrium with its surroundings [1-2]. The principles of thermodynamics allow us to derive and describe the relationships among the state variables (temperature T, pressure P, volume V, and entropy S) and thermodynamic potentials (internal energy U, enthalpy H, Gibbs free energy G, and Helmholtz F) in an open or closed system. The relationship between the state variables and thermodynamic potentials can be defined by differential and partial differential equations [3]. To recall the position of state variables and the relationship between thermodynamic functions, different mnemonic schemes have been developed in the literature [4-8]. Max Born square is one of the mnemonic schemes, which acts based on the sentence: "Good Physicists Have Studied Under Very Fine Teachers".

The first letters of the mentioned sentence show the arrangement of G-P-H-S-U-V-F-T counterclockwise starting from the six o'clock position, which is shown in Figure 1a.

The four thermodynamic potentials can be positioned between their corresponding state variables. As shown in Figure 1b, the two arrows are drawn towards the potential function, for example U, from the two far ends of the inner square diagonally to obtain dU. Thus, the differential equation for U is obtained by dU = (+T) dS+ (-P) dV, where the variables (S and V) are close to the thermodynamic potential parameter (U). The variables of states are applied with the two arrows as a memory aid for the positive and negative signs in the differential equation form of the thermodynamic potential. The sign of the state variable becomes positive when the direction of arrows is away from the variables. In contrast, its sign becomes negative when the direction of arrows toward the independent variable. The same arrows are used to obtain other Maxwell relations.

$$dU = T\,dS - P\,dV$$

$$\left(\frac{\partial T}{\partial V}\right)_S = -\left(\frac{\partial P}{\partial S}\right)_V$$
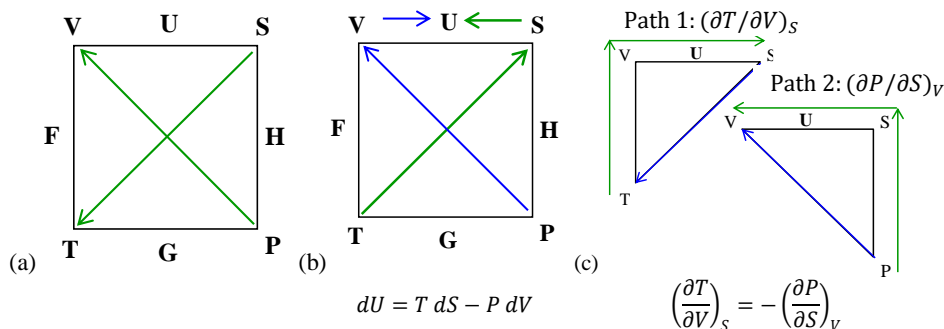
Figure 1. (a) Thermodynamic square presented by Max Born, (b), a scheme to recall the differential form of thermodynamic potentials (c), a scheme to obtain Maxwell relations.

As shown in Figure 1c, the Maxwell's relation is determined by following the arrows around one of the three corners of the square's sides, then following around its sides again in a reverse direction ending on the same side of the square. The sign of the Maxwell relation becomes negative when an endpoint has an arrow pointing to it, while the other does not, similar to $(\partial T/\partial V)_S = -(\partial P/\partial S)_V$.

Zhao [9] presented a modified mnemonic double-square scheme based on the Max Born square, in which the Max Born square is separated into two squares, an inner square that includes the state variables, and an outer square that contains the potentials, as shown in Figure 2a. The separation of variables from potential forms retains the advantage of the Max Born square, still it makes easier recalling of several sets of equations, including the Maxwell relations, without complicated rules to distinguish the negative or positive signs. In this method, the differential form of potentials is obtained by drawing two curved arrows toward the potential from the two far ends of the inner square crossing the inner square diagonally. As shown in Figure 2b, these two curved arrows give +TdS and -PdV for potential U form to obtain the differential form of internal energy, dU= TdS - PdV. The positive or negative sign of each term is determined by the upward or downward direction of the arrow crossing along the diagonal of the inner square. The Maxwell relations are determined by the inner square (state variables) without considering the outer (thermodynamic potentials) square, as shown in Figure 2c.

$$dU = T\,dS - P\,dV \qquad \left(\frac{\partial T}{\partial V}\right)_S = -\left(\frac{\partial P}{\partial S}\right)_V$$
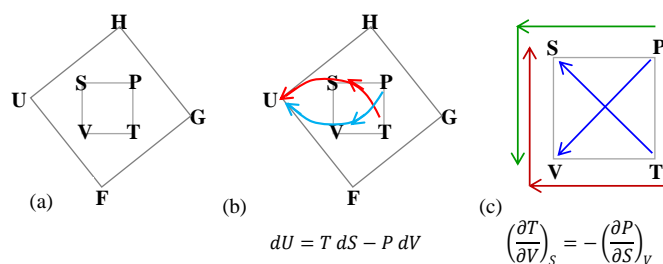
Figure 2. (a) Thermodynamic square presented by Zhao [7], (b) a scheme to recall the differential equations for thermodynamic potentials, and (c) Maxwell relations.

Each of Maxwell's relations is obtained by starting at any corner of the square scheme, going around the square either clockwise or counterclockwise for half a square by considering three variables each time. For example, we can start from T to V and then to S, which results $(\partial T/\partial V)_S$. The positive or negative sign of the term is determined by the upward or downward direction of the arrow connecting the first term letter (T) to the third term letter (S). As the arrow is upward, thus the term has a positive sign. The same procedure is used to obtain the other part of the Maxwell relationship $[-(\partial P/\partial S)_V]$.

The biggest advantage of this method is that the mode for positive and negative signs is modified compared to the Born square. Kerr and Macosko [10] proposed a "thermodynamic Venn diagram" [11] to derive the relations between the potentials and state variables of a simple system. The internal energy lies at the central point of the diagram, while the other thermodynamic potentials are positioned around the sides of internal energy. The Venn diagram is overlaid with two concentric "shading disks", and its differential form, which are shown in Figure 3a and 3b, respectively. The method for obtaining the Maxwell relations is the same as described for the thermodynamic square, but the state variables appear at

points across a circular arc rather than at the corners of the square. Therefore, there is a "shared arc" instead of the "shared second side".
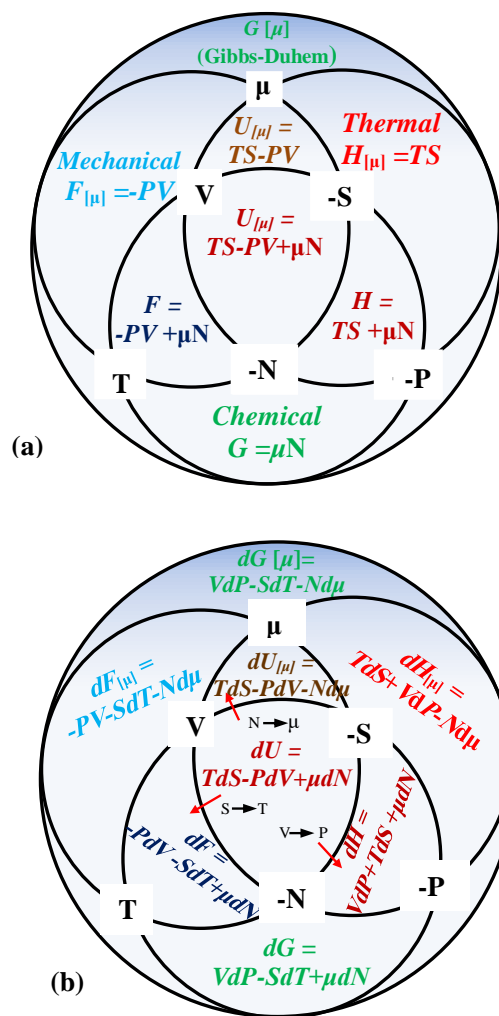
Figure 3. (a) Thermodynamic Venn diagram overlaid with two concentric "shading disks and (b) its differential form.

Although the Venn diagram method can well remember all the thermodynamic quantities, one of the most important problems of this method is that it takes a lot of time to draw, thus the speed of determining each of the thermodynamic quantities is slow. It is also necessary for the user to pay attention to the sign of the quantities and the direction of movement on each of the variables. In fact, if you don't pay attention to the arrows and the position of the parameters, it leads to choosing the wrong sign or the wrong differential form for each of the thermodynamic quantities.

Natarajan [12] proposed two simple mnemonic schemes, named "Natarajan's Thermodynamics circles", to present the Maxwell relations geometrically, which are easily used for both closed and open thermodynamic systems. The students' feedback was that they were able to organize the network of Maxwell thermodynamic relations in their minds carefully. Typically, the procedure for determining Maxwell's relation to potential U: $(\partial T/\partial V)_S = -(\partial P/\partial S)_V$ based on the "Natarajan's Thermodynamics circle" for a closed thermodynamic system is graphically shown in Figure 4. The start and end of the path that pass along the state variables which are from one of the first partial derivatives of Maxwell's relation are indicated by the number 1.

Figure 4. Graphical scheme for determining the Maxwell's relation for potential U: $(\partial T/\partial V)_S = -(\partial P/\partial S)_V$ based on the "Natarajan's thermodynamics circle" in a closed thermodynamic system [12].

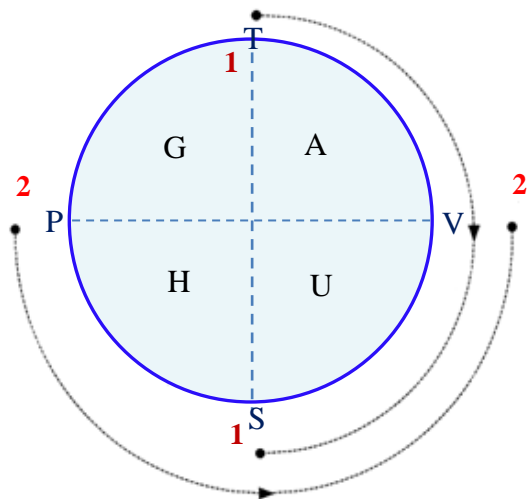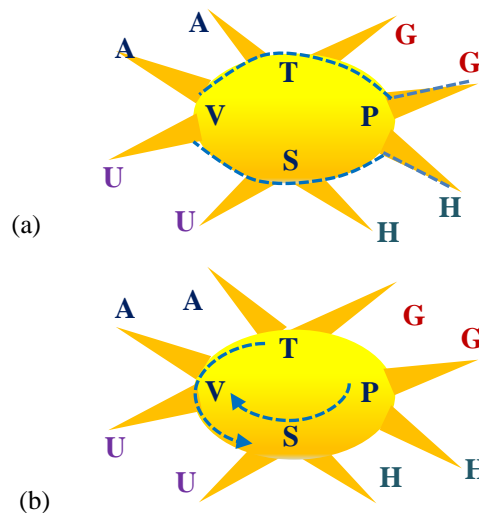Figure 5. Graphical schemes of (a) the variation of state variables and differential form of thermodynamic potentials by Fishing way, (b) Maxwell relations by swirl way [13].

Also, the start and end of the path that pass along the state variables, which are from one of the second partial derivatives of Maxwell's relation, are indicated by the number 2. The path directions are shown by the arrows. The sign of relations is considered positive and negative when the direction of the arrows is clockwise and counterclockwise, respectively. The Maxwell relations of other thermodynamic potentials (H, G, and A) can be derived from the "Natarajan's thermodynamic circle".

One of the most common mistakes that may occur in obtaining thermodynamic relationships based on the previous methods is not considering the sign/direction of a formula. Recently, Bhagavanbhai et al. [13] proposed a simple set of rules, named "Fishing with scissors" mnemonic, to cover fundamental thermodynamic equations, Maxwell's relations of thermodynamic potentials with state variables. This method was free from the direction/sign related difficulties that were reported in the previous methods. The graphical schemes for determining (a) the relationship between state variables and partial differential equations of thermodynamic potentials by "Fishing way", and (b) Maxwell's relations by "swirl way" are shown in Figure 5. In the "Fishing way", the relation between thermodynamic potentials and state variables was obtained from tail to mouth of fish as guided by a dashed line (Figure 5a). For example, we can start from G to P and then to T and finally to V, which results $(\partial G/\partial P)_T = V$.

In the swirl way, named up-directed and down directed swirls, the Maxwell relations are determined based on the picking up the state terms from sun region in two counter ways (as guided by dashed lines) such that first counter cover vertical half terms of sun, while second counter way horizontal half terms of sun (Figure 5b), which result $(\partial T/\partial V)_S = -(\partial P/\partial S)_V$.

In the present study, we proposed a novel and simple method to derive the classical equations in thermodynamics potentials and Maxwell relations based on the butterfly symmetry method for a closed thermodynamic system. The proposed methodology has solved the problems caused by the arrangement and sign of parameters, which were reported in the other mnemonic procedures such as square, Venn diagrams, and Natarajan's thermodynamics circle.

2. Results of Proposed Methodology
2.1. Relationship between Thermodynamic Potentials and State Variables

According to Figure 6, at first, each of the state variables (T, P, S, and V) are placed on the vertical and horizontal axes of the table, respectively. The thermodynamic potentials are placed from the bottom and counter-clockwise in the order of G, U, H and F. To help remember the position of the potentials, the first letter from the sentence of: "Good Understand, Highly Favorite" is used in the side of table. Two middle columns have a positive sign and the two side columns have a negative sign (Figure 6b).

According to Figure 6b, we cross the yellow columns diagonally (according to the green arrow) to determine the relationship between F and U. When passing through each of the columns, we also include the positive or negative sign of that column. For example, to determine the relationship between F and U with related state variables, we have: $F = U - TS$. In addition, for H and G we have: $H = G + TS$.

To determine the relationship between H and U, and also G and F, it is necessary for the sides to make a butterfly form through the vertical dashed lines (according to the red arrow) and consider the parameters in the yellow columns with the related sign. The end of the arrow indicates the desired state variables that must be put in the equation. Therefore, to determine the relationship between U and H, while passing through the $-PV$ column, we will have: $U = H - PV$. Similarly, the relationship between G and F, while passing through the $+PV$ column, leads to $G = F + PV$ (Figure 6b).

2.2. Determination of The Differential Form of Thermodynamic Potentials

According to Figure 7, at first, each of the state variables (T, P, S, and V) and the differential form of each of the mentioned quantities are placed on the vertical and horizontal axes of the table, respectively. The differential form of the thermodynamic potentials is placed from the bottom and counter-clockwise in the order of G, U, H and F.

The formation of the butterfly symmetry mode starts from dU and reaches dH, and then dG and finally dF. By moving along the horizontal line that connects F to U leads to drawing a symmetrical butterfly form.
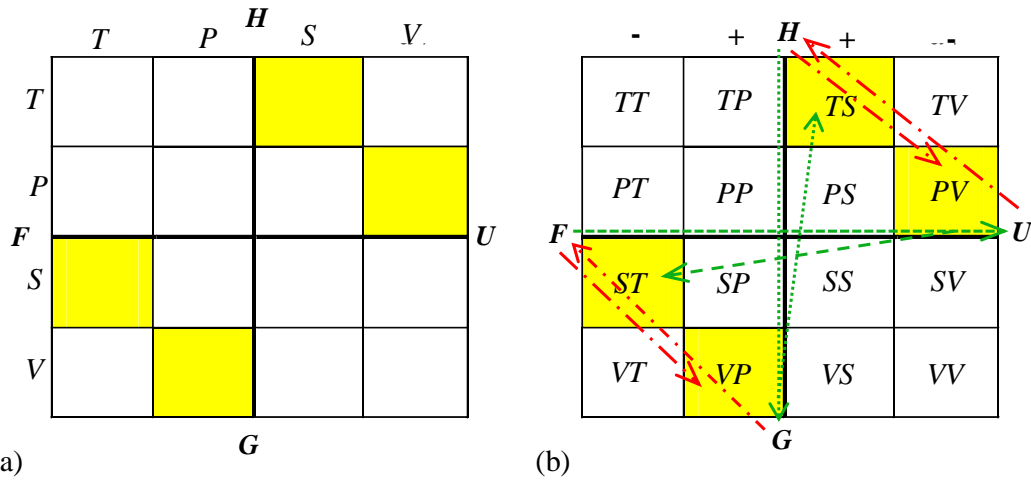
Figure 6. Scheme to obtain the relationship between thermodynamic potentials and the state variables.
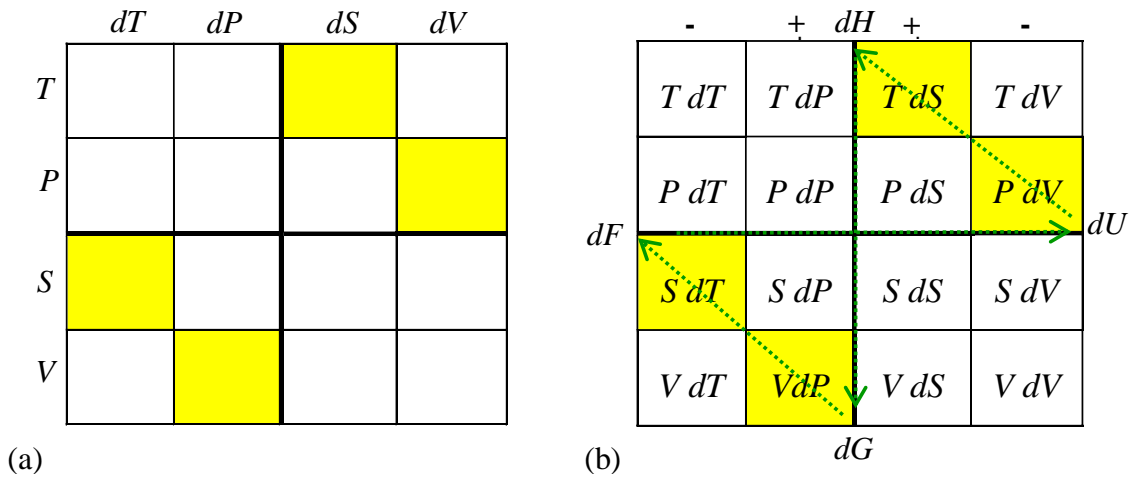
Figure 7. Scheme to obtain the differential form of thermodynamic potentials with state variables.

For example, to determine the differential form of U according to Figure 7b, we cross the yellow columns diagonally (according to the green arrow). When passing through each of the columns, we also include the positive or negative sign of that column. For dU we have: $dU = -PdV + TdS$. Other thermodynamic quantities are determined similarly to this method. To determine the differential form of H, it is necessary to move down from the vertical line and consider the parameters in the yellow columns with the mentioned sign. Therefore, to determine dH while passing through the $+TdS$ and $+VdP$ columns, we will have: $dH = +TdS + VdP$. The differential form of G is similar to U, and to determine F, it is similar to H.

2.3. Proposed Scheme to Obtain The Maxwell Relations

Figure 8 shows the scheme to recall the differential equations for thermodynamic potentials obtained from the state variables. Each of the state variables is fixed, and the relative derivative form of each of the mentioned quantities is placed on the horizontal axis in the mentioned order. Derivative changes are made with respect to S, V, T and P. The slanted green line, shown in Figure 8b, shows the axis of symmetry. In this way, by equalizing each of the relative derivative states placed at the two ends of the line according to the arrows, each of Maxwell's relations with their signs is formed two by two. For example, we have $-(\partial S /\partial V)_T = (\partial P/\partial T)_V$. Other Maxwell relations are determined in the same way.

Figure 8. Scheme to obtain the differential equations form of state variables.

3. Conclusions

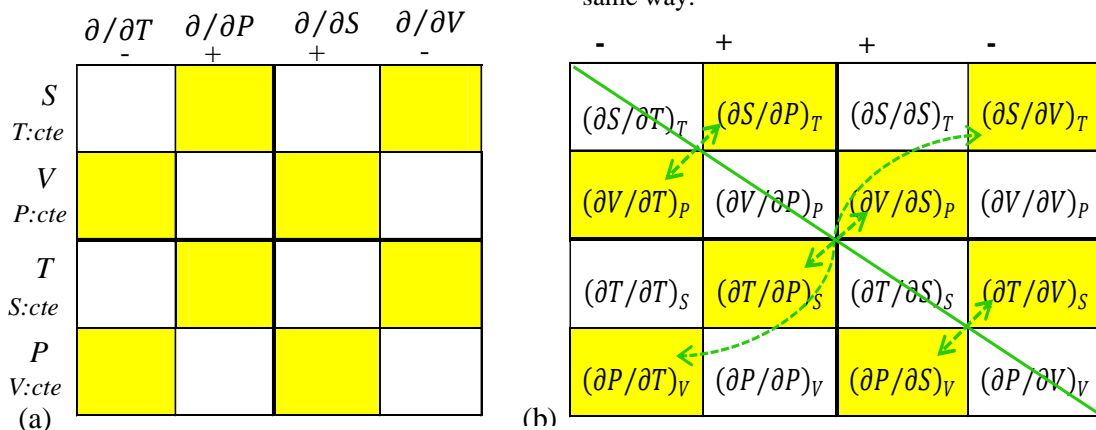A mnemonic scheme based on the butterfly symmetry method is suggested to derive classical thermodynamics potentials that connect the state variables and Maxwell's relations in a closed thermodynamic system. This method resolves the identical elements and Maxwell's formulas in the energy, enthalpy, Helmholtz and Gibbs equations by creating a matrix. The most important feature of this method is that the differential and partial derivatives of thermodynamic quantities are formed in matrix arrays. The proposed method does not have the difficulties caused by the arrangement and sign of parameters in the square, cub octahedron, concentric multi-circle, Venn diagrams, and "Natarajan's thermodynamics circles". In addition, the signs are applied only according to the butterfly symmetry, and unlike the Max Born method, there is no need to pay attention to the direction of arrows, which helps to make it easy for students to learn.

References:

[1] J. F. Le Marechal and R. El Bilani, "Teaching and Learning Chemical Thermodynamics in School," *International Journal of Thermodynamics*, vol. 11, no. 2, pp. 91-99, Jun. 2008, doi: 10.5541/ijot.216.

[2] M. V. Zemansky. *Heat and Thermodynamics*, New York: McGraw-Hill, 1968.

[3] L. Tisza. *Generalized Thermodynamics*, Cambridge: MIT Press, 1966.

[4] D. E. Christie. "Multipurpose mnemonic for thermodynamic equations," *American Journal of Phys*ics, vol. 25, no. 1, pp. 486-487, Oct. 1957, doi: 10.1119/1.1934516.

[5] F. O. Koenig. "Families of thermodynamic equations. I The method of transformations by the characteristic group," The *Journal of Chemical Physics*, vol. 3, no. 1, pp. 29-35, Jan. 1935, doi: 10.1063/1.1749549.

[6] H. B. Callen. *Thermodynamics: An introduction to physical theories of equilibrium thermostatic and irreversible thermodynamics*, New York: John Wiley & Sons Inc, 1960.

[7] S. F. Pate. "The thermodynamic cube: A mnemonic and learning device for students of classical thermodynamics," *American Journal of Physics*, vol. 67, no. 1, pp. 1111-1113, Dec. 1999, doi: 10.1119/1.19093.

[8] J. E. Fieberg and Ch. A. Girard. "Mnemonic device for relating the eight thermodynamic state variables: The energy pie," *Journal of Chemical Education*, vol. 88, no. 11, pp. 1544-1546, Aug. 2011, doi: 10.1021/ed100902z.

[9] J. C. Zhao. "A mnemonic scheme for thermodynamics," *MRS Bulletin,* vol. 34, no. 2, pp. 92-94, Feb. 2009, doi: 10.1557/mrs2009.26.

[10] W. C. Kerr and J. C. Macosko. "Thermodynamic Venn diagrams: Sorting out forces, fluxes, and Legendre transforms," *American Journal of Phys*ics, vol. 79, no. 9, pp. 950-953, Sep. 2011, doi: 10.1119/1.3599177.

[11] J. Venn. "On the diagrammatic and mechanical representation of propositions and reasoning," *Philosophical Magazine Series 5*, vol. 58, no. 10, pp. 1-18, Jul. 1880, doi: 10.1080/14786448008626877.

[12] K. Natarajan. "Graphical summaries for Maxwell relations of closed and open thermodynamic systems," *International Journal of Mechanical Engineering Education,* vol. 42, no. 1, pp. 1-17, Jul. 2014, doi: 10.7227/IJMEE.42.1.1.

[13] G. G. Bhagavanbhai, J. J. Bravo-Suarez and R. Kumar. "Fishing with scissors: A mnemonic for thermodynamic formula," *Oriental Journal of Chemistry*, vol. 37, no. 3, pp. 700-703, May 2021, doi: 10.13005/ojc/370326.

Research Article

Investigation of Photovoltaic Membrane Desalination Utilizing Storage Heat in Solar Cells

[1*] H. A. Abdul Kareem (ID), [1] A. N. Khalifa (ID), [1] A. J. Hamad (ID)

[1] Middle Technical University, Engineering Technical College- Baghdad
E-mail: [1*] huseinali1987@gmail.com

Abstract

Solar-assisted Photovoltaic-Membrane Distillation (PMD) is a passive tool to cool and distillate salty water. A theoretical study was conducted in the current work using the COMSOL Multiphysics version 5.6 to develop the CFD model of the PMD. The meteorological data of Baghdad- Iraq was obtained using Meteonorm software V8.0.3.Effects of membrane thickness, space between evaporation and condensation layer, height of fins, number of fins, and inlet water temperature on cell temperature and water productivity were investigated. Thickness of 100 μm exhibited a minimum temperature polarization and maximum membrane coefficient. Space thickness of 2.5 mm exhibited a temperature difference of 4°C between evaporation and condensation layers. Integrating the PMD system into solar panel reduced the cell surface temperature by 7°C. Adding a heat sink of 5 fins with a fin height of 2 cm resulted in a maximum cell temperature of 50 °C and yielded water at point 0.615 kg/h.m² rate.

Keywords: Membrane distillation; CFD simulations; cooling solar PV panels; green technology.

1. Introduction

The world has turned to search for renewable and clean energy that is environmentally friendly due to the massive consumption of fossil fuels that leads to ozone layer depletion and global warming. Among renewable energies, solar energy, especially PV solar systems, is a promising energy that can subsidize and reduce the consumption of fossil fuels. The conversion of solar energy into power in solar cells is shallow and is about 14 to 18%. The rest of the solar energy is solar radiation that has not been converted into energy which stored in the solar cell as thermal energy and causing a rise in the cell's temperature. The high cell temperature negatively impacts cell performance and reduces the cell's life span. The deviation from the cell's standard operating conditions and the PV panel conversion efficiency are decreased by 0.4 to 0.5% per 1 °C[1].

Rabie et al. 2022[2] introduced the hybridization of high-concentrating photovoltaic (HCPV) with membrane distillation (MD). Numerically, membrane distillation was introduced experimentally. The study aimed to keep the cell's temperature within the standard temperature design. Aleid, 2019 [3] studied effect of membrane thickness on water productivity, three stages of MDS models were investigated. Shi Y et al. 2019 [4] used a photovoltaic-membrane distillation device that can simultaneously produces a clean water and power from the solar energy. Zhao et al. 2020 [5] studied integration of a photovoltaic module (PVM) integrated with a direct contact membrane distillation system (DCMD). The heat generated in the PV panels was used for water pureness. A mathematical model for both DCMD and PVM was proposed, and the numerical results were validated by comparing them with the experiment. Kumar, 2015 [6] proposed a solar distillation system to supply a potable water to urban settlements by combining solar-powered hot water installations with water purification systems. Chiavazzo et al. 2018 [7] proposed a low-cost multistage solar distiller that operates on one sun irradiance. The unit stage was built from three layers; the first and third layers are called hydrophilic, and the second was a hydrophobic microporous membrane. Baloch et al. 2015 [8] Cell surface cooling was experimental and numerical investigated. The simulation model was built using the ANSYS-Fluent software of version 6.3. Popovici et al.2016 [9] introduced a numerical study for reducing the photovoltaic panel's temperature using an air-cooled heat sinks. The heat sink was conceived as a ribbed wall and consisted of a with high thermal conductivity material. Li et al. 2020 [10] developed a novel PV solar-powered stand-alone sweeping gas membrane desalination system. A solar thermal collector was installed for thermal energy collection, and a PV solar array was established to generate AC power. Wang et al. 2020 [11] tested a multistage membrane distillation device (MSMD) and installed it at a back of solar panel. The 5-stage photovoltaics-membrane distillation-evaporative crystallizer (PV-MD-EC) system showed that the productivity of such a system was around 2.45 kg/h.m², with a lower solar cell temperature of 48℃.

In the current work, a Photovoltaics-membrane distillation unit (PMD) was modeled and simulated using the COMSOL Multiphysics 5.6 software. Modeling of the PVM unit was applied on July 1st which is considered the hottest day in Baghdad- Iraq (33.3 ° N, 44.14° N, and 34 m elevation) . In the current work, a Photovoltaics-membrane distillation unit (PMD) was modeled and simulated using the

---

COMSOL Multiphysics 5.6 software. Modeling of PVM unit was applied in 1-July, which is considered the hottest day in Baghdad- Iraq, with a 33.3 ° N, 44.14° N, and 34 m elevation. A passive method was used to cool a PV cell, where a heat generated in the cell and rejected outside using different fluids such as water or air. Issue of storing the heat in the cells was studied. This heat was used for two purposes: cooling the solar panel and desalinating brackish water. Effects of membrane thickness, space between evaporation and condensation layer, height of the fins, number of fins, and inlet water temperature on the cell temperature and water productivity were investigated.

2. Module Description

The PMD system commonly consists of single or multistage. Each stage consists of several layers of hydrophilic membranes working as evaporators or condensers. The principle of any PMD system is to minimize distance between the thin hydrophilic layers; thus, cycle of evaporation and condensation processes was carried out at ambient pressure. Figure 1 shows a single-stage PMD, where the hydrophilic (evaporation layer) adheres directly to the aluminum plate, directly in contact with the back of the solar panel. Water was supplied to the PMD unit by pumping or gravity force; the evaporator layer was wetted by capillary action. The first aluminum plate transfers generated heat in the PV panel to the salty water. In contrast, the last aluminum layer comes into contact with the heat sink to dissipate the accumulated heat in the PV panel as latent heat of evaporation. The salty water comes into contact with the first hot aluminum layer; hence, part of the salty water evaporates and transfers through the steel mesh layer and the membrane, and finally, reaches the condensing layer. In the condenser layer, the vapor condensate to a fresh water and lose the latent heat of evaporation to the aluminum plate in the multistage system or to the heat sink in the single-stage system. For each case, the heat sink was placed at the last cooling stage. Table 1 shows dimensions of the PMD layers. Salinity of salty water was about 400 PPM.
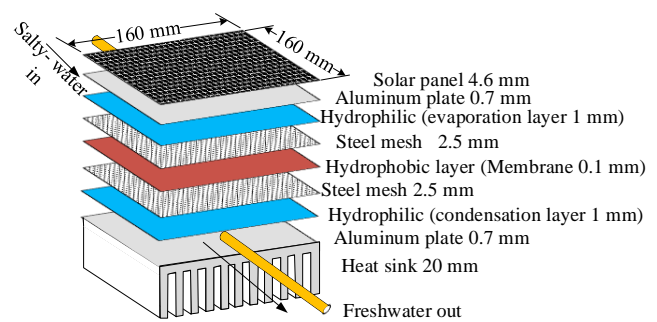

Figure 1. Schematic diagram of PMD system.

3. PMD System Simulation Model

The COMSOL Multiphysics version 5.6 was used to develop the CFD model of the PMD. Meteorological data for Baghdad- Iraq, including global solar radiation and ambient temperature, was obtained from Metronome software V8.0.3. Governing equations, assumptions, and boundary conditions were mentioned in the next section. Three temperature values were calculated for the PMD unit; back cell surface temperature (T_{Cell}), hydrophilic evaporation layer temperature (T_{Evap}) and hydrophilic condensation layer temperature (T_{Cond}), as shown in Figure 2. Two kinds of mesh generators were utilized in implementing the model. The first type was a free normal triangular mesh which was designed for the solar panels, aluminum plates and fins, with a maximum element size of 0.62 m. The second type was free extra fine element-size triangular mesh, which was utilized for domain of laminar flow (evaporation and condensation layers and hydrophobic membrane. The maximum element size for this type was 0.557m, and the number of elements for the PVM model was 712760, as shown in Figure 3. Normally, the residuals for the converged numerical solution are illustrated in Figure 4. Moreover, Figure 5 shows the structure of the COMSOL computation processes.

Table 1. Dimensions of the PMD model layers.

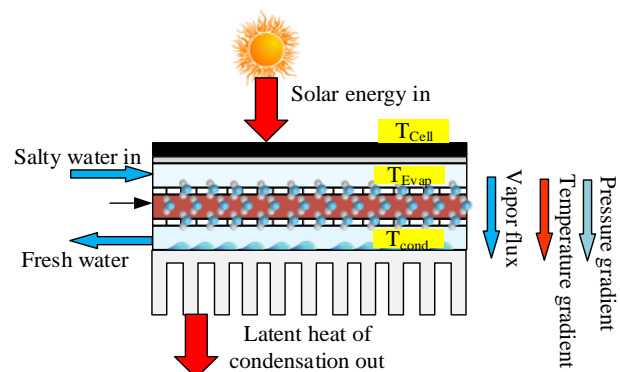| Dimension	Value
Solar cell	16×16×0.46 cm
Aluminum sheet (two layers)	16×16×0.07 cm
Hydrophilic layer (evaporation)	16×16×0.1 cm
Steel mesh (two layers)	16×16×0.25 cm
Hydrophobic layer membrane	16×16×0.01 cm
Hydrophilic layer (condensation)	16×16×0.1 cm
Inlet and outlet water tube diameter	0.035 cm
heat sink	5 fins, 2cm high

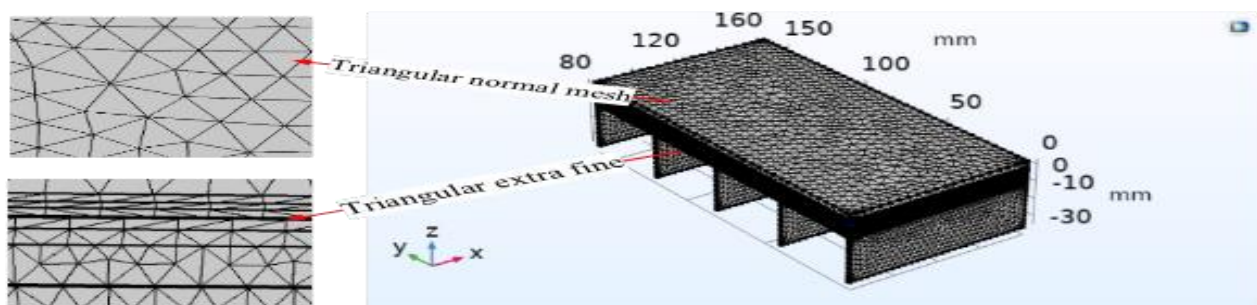*Figure 2. Schematic diagram of the PMD system.*

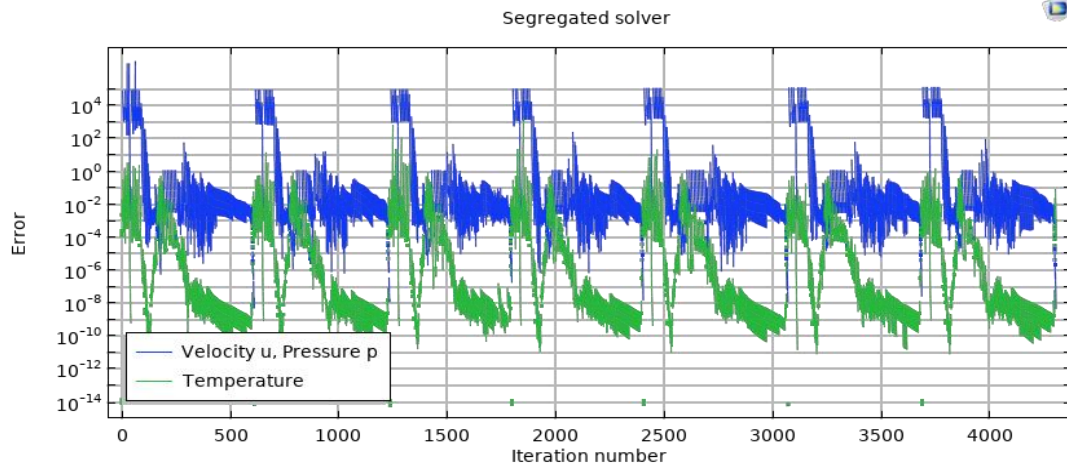

Figure 3. Mesh of the PMD system.

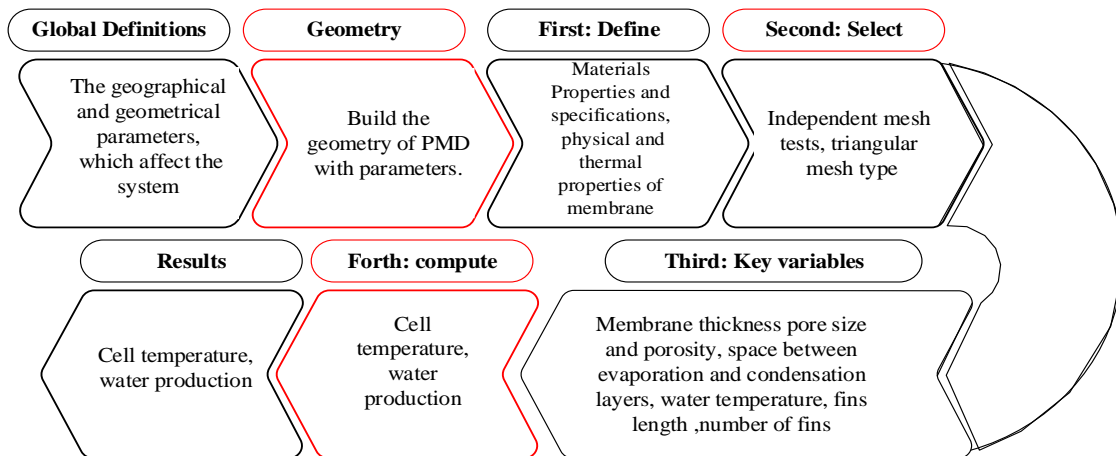*Figure 4. Residuals for the converged numerical solution.*

Figure 5. Structure of the COMSOL computation processes in detail.

3.1 Materials Properties and Specifications

The input physical characteristics of materials used in the PMD model were specified using the COMSOL database, and all the properties are listed in Table 2 as follows:

1. The solar panel consisted of five layers: a glass covering, two layers of ethylene-vinyl acetate (EVA), silicon, and a back sheet layer (Tedlar). The input properties were; thermal conductivity (k), coefficient of thermal expansion (α_{iso}) and specific heat (c_p).

2. Water was used for both evaporation layer and condensation layer. The input properties were water density (ρ), water-specific heat (cp) and thermal conductivity (k). All the properties temperature dependent. This layer is consisted of fluid and matrix properties and porous medium permeability(δ). The porosity of mesh is 80%, and the pore size was 25μm.

3. Polytetrafluoroethylene (PTFE) was used as a membrane material. The pore size was 0.45 μm, and the porosity was about of 85%. The input properties were; density(ρ), specific heat (cp) and thermal conductivity (k).

4. Aluminum was used as a conductive and heat sinks material. The input properties were; specific heat (c_p) and thermal conductivity (k).

3.2 Assumptions

The following assumptions were considered in the formulation of the present PMD simulation model:

1. Incompressible and laminar fluid flow through membrane channels.

2. Unsteady state condition with three-dimensional heat transfer for the computational domain.

3. Thermo-physical properties of the fluid were considered as a temperature-dependent.

4. The physical characteristics of the PTFE membrane, density, viscosity, heat capacity and thermal conductivity, were assumed as constant values.

5. The vapor phase was considered as an ideal gas, while the liquid phase was an ideal solution.

6. The temperature of the ambient and solar radiation was time-dependent.

7. The PMD system was perfectly insulated, and the energy loss was neglected negligible.

Table 2.[12] *Thermophysical properties of PV panel and PMD layers.*

No	Material	Thermal conductivity (W/m K)	Density (kg/m³)	Specific heat (J/kg.K)	Specific heat (J/kg.K)
1	Water	0.625	991	4172	4172
2	PTFE	0.24	2200	1050	1050
3	Silicon	148	2330	677	677
4	EVA	0.35	960	2090	2090
5	Glass	1.8	3000	500	500
6	Tedlar	0.2	1200	1250	1250
7	Aluminum	238	2700	900	900

3.3 Governing Equations

The conservation equations of mass, momentum and energy were the basis of the governing equations used to determine velocity, pressure and temperature distributions in the computational domain of the PMD simulation model. The equations can be written as follows [13], [14],[15]:

I- Conservation equations for non-permeable layers in the PMD system (PV solar panel, Aluminum plate, fins) can be expressed by continuity equations as follows:

$$\frac{\partial \rho}{\partial t} + \rho \left(\frac{\partial u}{\partial x} + \frac{\partial v}{\partial y} + \frac{\partial w}{\partial z} \right) = 0 \qquad (1)$$

Momentum equation:

$$\rho \frac{\partial u}{\partial t} + \rho(u\frac{\partial u}{\partial x} + u\frac{\partial v}{\partial y} + u\frac{\partial w}{\partial z}) = \mu(\frac{\partial^2 u}{\partial x^2} + \frac{\partial^2 u}{\partial y^2} + \frac{\partial^2 u}{\partial z^2}) + \rho g - \frac{\partial P}{\partial x} \qquad (2)$$

$$\rho \frac{\partial v}{\partial t} + \rho(v\frac{\partial u}{\partial x} + v\frac{\partial v}{\partial y} + v\frac{\partial w}{\partial z}) = \mu(\frac{\partial^2 v}{\partial x^2} + \frac{\partial^2 v}{\partial y^2} + \frac{\partial^2 v}{\partial z^2}) + \rho g - \frac{\partial P}{\partial y} \qquad (3)$$

$$\rho \frac{\partial w}{\partial t} + \rho(w\frac{\partial u}{\partial x} + w\frac{\partial v}{\partial y} + w\frac{\partial w}{\partial z}) = \mu(\frac{\partial^2 w}{\partial x^2} + \frac{\partial^2 w}{\partial y^2} + \frac{\partial^2 w}{\partial z^2}) + \rho g - \frac{\partial P}{\partial z} \qquad (4)$$

Energy equation:
For fluid flow and solar PV pa0nels, the energy equations are:

$$\rho \, C_P \frac{\partial T}{\partial t} + \rho \, C_P \left(u \frac{\partial T}{\partial x} + v \frac{\partial T}{\partial y} + w \frac{\partial T}{\partial z} \right) = k \left(\frac{\partial^2 T}{\partial x^2} + \frac{\partial^2 T}{\partial y^2} + \frac{\partial^2 T}{\partial z^2} \right) + Q_{in} \qquad (5)$$

$$\rho \, C_p \frac{\partial T}{\partial t} = k \left(\frac{\partial^2 T}{\partial x^2} + \frac{\partial^2 T}{\partial y^2} + \frac{\partial^2 T}{\partial z^2} \right) \qquad (6)$$

II- Conservation equations for permeable layers in the *PMD* system (membrane and micro-channels) of the PMD system can be expressed by continuity equation [15]:

$$\frac{1}{\epsilon}\frac{\partial \rho}{\partial t} + \rho \left(\frac{\partial u}{\partial x} + \frac{\partial v}{\partial y} + \frac{\partial w}{\partial z} \right) = 0 \qquad (7)$$

Momentum equation:

$$\frac{1}{\epsilon}\rho \frac{\partial u}{\partial t} + \frac{1}{\epsilon^2}\rho \left(u\frac{\partial u}{\partial x} + v\frac{\partial u}{\partial y} + w\frac{\partial u}{\partial z} \right) = -\frac{\partial p}{\partial x} + \frac{\mu}{\epsilon} + \frac{\partial^2 u}{\partial x^2} + \frac{\partial^2 u}{\partial y^2} + \frac{\partial^2 u}{\partial z^2}$$
$$-\frac{\mu}{K}u - \frac{\rho_f C_f}{\sqrt{K}}\,/u/u \qquad (8)$$

$$\frac{1}{\epsilon}\rho \frac{\partial v}{\partial t} + \frac{1}{\epsilon^2}\rho \left(u\frac{\partial v}{\partial x} + v\frac{\partial v}{\partial y} + w\frac{\partial v}{\partial z} \right) = -\frac{\partial p}{\partial y} + \frac{\mu}{\epsilon} \left(\frac{\partial^2 v}{\partial x^2} + \frac{\partial^2 v}{\partial y^2} + \frac{\partial^2 v}{\partial z^2} \right) - \frac{\mu}{K}v - \frac{\rho_f Cf}{\sqrt{K}}|v|v \qquad (9)$$

$$\frac{1}{\epsilon}\rho \frac{\partial w}{\partial t} + \frac{1}{\epsilon^2}\rho \left(u\frac{\partial w}{\partial x} + v\frac{\partial w}{\partial y} + w\frac{\partial w}{\partial z} \right) = -\frac{\partial p}{\partial z} + \frac{\mu}{\epsilon} \left(\frac{\partial^2 w}{\partial x^2} + \frac{\partial^2 w}{\partial y^2} + \frac{\partial^2 w}{\partial z^2} \right) - \frac{\mu}{K}w - \frac{\rho_f Cf}{\sqrt{K}}|w|w \qquad (10)$$

Energy equation:

$$c_p\epsilon\frac{\partial T}{\partial t} + \rho \, c_p \left(u\frac{\partial T}{\partial x} + v\frac{\partial T}{\partial y} + w\frac{\partial T}{\partial z} \right) = k_{f,eff}\left(\frac{\partial^2 T}{\partial x^2} + \frac{\partial^2 T}{\partial y^2} + \frac{\partial^2 T}{\partial z^2} \right)$$
$$+ h_{sf} \, a_{sf} \, (T_s - T_f) \qquad (11)$$

3.4 Calculation of The Production Rate of Clean Water:

According to the membrane distillation theory, the clean water production rate (or vapor flux) that passes through the porous hydrophobic membrane depends on the membrane coefficient and the difference of vapor pressure between the evaporation and condensation layers. The following formula is used to calculate the rate of production:

$$J = \Delta p * c_m \qquad (12)$$

The Antoine equation is used to determine the relationship between temperature and vapor pressure (*P*) in the condensation and evaporation layers [15]:

$$P = \exp\left(A - \frac{B}{C+T} \right) \qquad (13)$$

Where A, B, and C for water are constants of values 23.238, 3841, and -45, respectively [15]. Vapor pressure is denoted by *P* (bar), and temperature by T (K).

The following equation may be used to compute the membrane coefficient(c_m) [16]:

$$c_m = \frac{1}{\frac{3}{2}*\frac{\omega*\delta}{\epsilon*r}*\left(\frac{\pi*R_o*T}{8M}\right)^{0.5} + \frac{\tau*\delta}{\epsilon}*\frac{P_a}{p.D}*\frac{R*T}{M}} \qquad (14)$$

Where: M= molecular weight of the water $(18.02 \frac{kg}{mol})$, R_o= is the gas constant, $R_o = 8.314 \frac{kJ}{mol\,K}$ and r is pour size of membrane.

The following equation may be used to compute the water-air PD and pore tortuosity [17]:

$$P.D = 1.895 * 10^{-5} * T^{2.072} \qquad (15)$$

$$\omega = \text{pore tortuosity} = \left(\frac{2-\epsilon}{\epsilon} \right)^2 \qquad (16)$$

permeability of porous media is determined by [18]:

$$\delta = 8.5 * (\epsilon * r^2)^{1.3} \qquad (17)$$

4. Operating Parameters and Boundary Conditions
4.1 The Geographical and Geometrical Parameters:

The effect of membrane thickness, the space between the evaporation and condensation layer, the height of the fins, the number of fins, and the inlet water temperature on the cell temperature and water productivity were investigated.

4.2 Boundary Conditions:

Based on the computational domain shown in Figure 6, the boundary conditions for fluid and solid walls were assumed as follows:

Solid surface (Walls): No slip condition on solid walls (u= 0, v= 0, w= 0).No thermal jump on the wall. Adiabatic condition for insulated surfaces (q= 0, or dq= 0).

Membrane: The boundary walls were considered as non-slip conditions, and the sides of the membrane layers were assumed to be thermally insulated. The interfaces between the membrane and the channels were considered coupled interfaces.

Solar pane PV: The PV panel's top surface was subjected to a solar radiation G (W/m²). Convection and radiation heat transfer occurs at the top surface of the PV panel. Conductive heat transfer occurs through the layers of solar PV panels, with negligible thermal contact resistances between the panel layers.

The aluminum sheet: which was attached to the back surface of the solar PV panel, was assumed to be a heat sink with a perfect contact with the back of the PV panel.
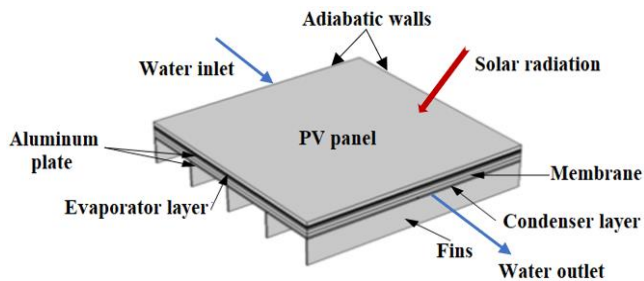
Figure 6. Boundary conditions of the PVM model computational domain.

5. Result and Discussions

It is worth noting that all the cases reviewed have two factors that affect the performance of the cell: the first is cell temperature, and the second is cell water productivity. Although the two factors are essential, the cell temperature is considered to be the critical factor. Value of mass flow rate of the supply water was assumed to be equal to 0.856 kg/h.m^2 according to Wang et al. [19]. Weather conditions of Baghdad (33.3152° N, 44.3661° E), in which the experiments were conducted, are shown in Figure 7.
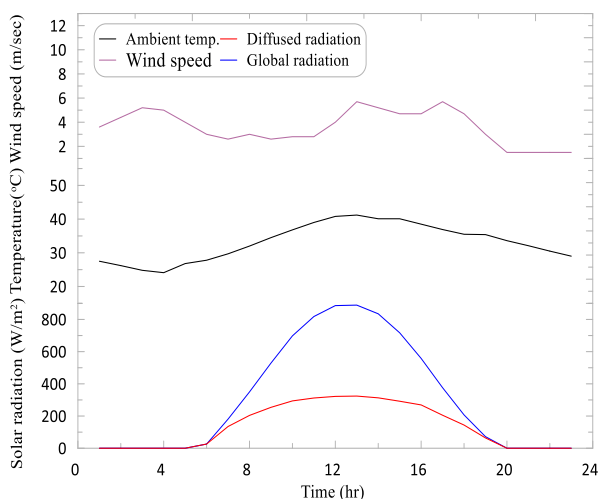

Figure 7. Baghdad Weather conditions.

Validation of the membrane coefficient of the current work with Aleid et al. [3] is shown in Figure 8. The deviation between the two works was about 8%. Moreover, Figure 9 illustrates a comparison between the current theoretical study with Wang et al. [19] the results indicated that the intensity of solar radiation was, approximately, identical for both the studies. However, the difference was observed in the ambient temperature, where, Wang's work exhibited a higher temperature than the current work. This suggests that an increase in cell temperature was observed in the current work. The temperature difference between the cell and the environment was nearly the same in both studies, with an error rate ranging between -1.5 to 4.4%.

The effect of the membrane thickness ranged from 100 to 1000 μm on the temperature polarization for the condensation and evaporation layer is shown in Figure 10. Increasing the membrane thickness increased the temperature of polarization. It clearly observed that the temperature of polarization tended to reduce the difference in the vapor pressure across the membrane.

Figure 11 shows the relation between the membrane thickness and the membrane coefficient (The vapor permeability through the membrane). The results indicated

that the thin membrane exhibited a higher membrane coefficient.
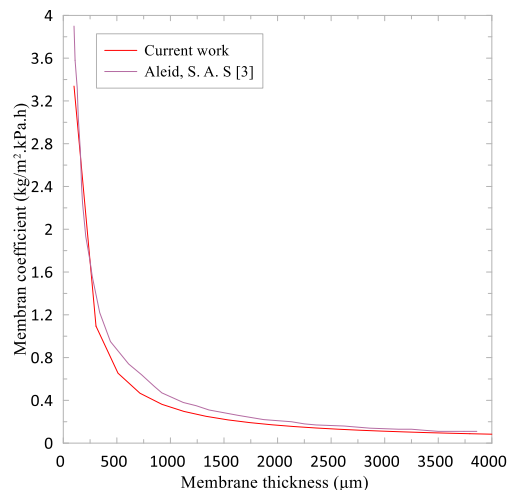
Figure 8. Validation of membrane coefficient.
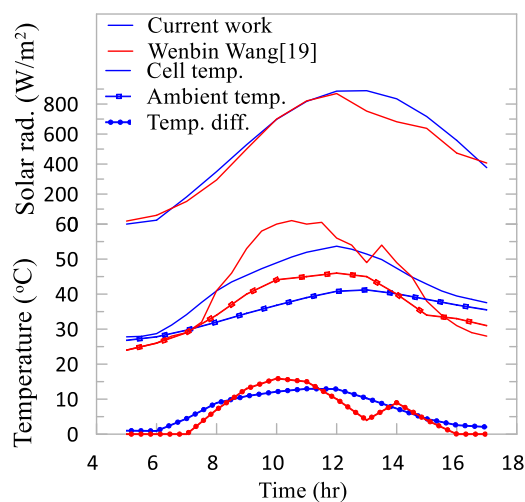
Figure 9. Validation of current work with experiment work.
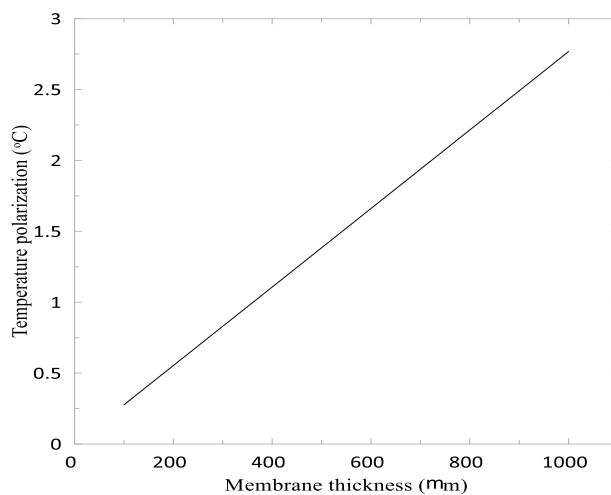
Figure 10. Effect of membrane thickness on the temperature polarization (°C).

Space thickness between the evaporation and condensation layers is a critical factor for providing the temperature difference between evaporation and condensation layers. This temperature difference creates a pressure difference that drives water vapor movement evaporation to condensation layers. This distance can be carried out using two ways: by placing hydrophobic

membranes between them or by placing a mesh [7]. The two methods are adopted to ensure space between the condenser and the evaporator layers. Figures 12 and 13 show the effect of space thickness on the evaporation and condensation temperature. The figures show that the space thickness affects the evaporation temperature more than the condensing temperature. However, the 2.5- and 3-mm space thicknesses show higher evaporation temperatures. The same trends in the first half of the day are observed for the two space thicknesses mentioned. From an economic perspective, the space thickness of 2.5 mm was adopted in the current work.Figure 14 shows the difference between evaporation and condensing temperature for 2.5 mm space thickness. There is no difference between the evaporation and condensing temperatures at night. In daylight time, the difference between the two temperatures rises and reaches a maximum value at noon. Figure 15 shows the effect of the integration of PMD and the PV panel on the cell surface temperature at a space thickness of 2.5 mm. The maximum difference between the cooled and uncooled cell temperatures was about of 7°C at solar noon. The reduction in cell temperature was due to the absorption of cell-stored heat by the water supply.
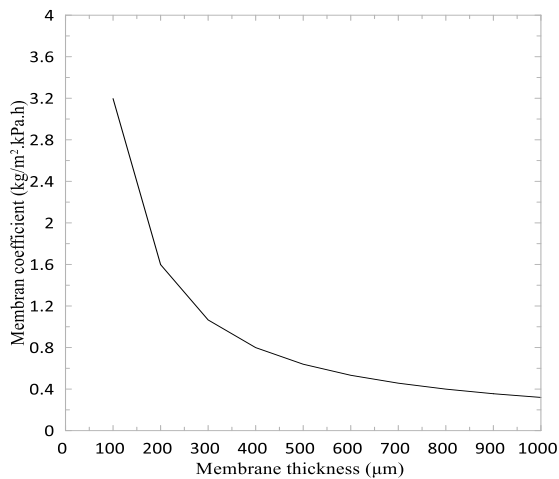
Figure 11. Relation between the membrane thickness and membrane coefficient.
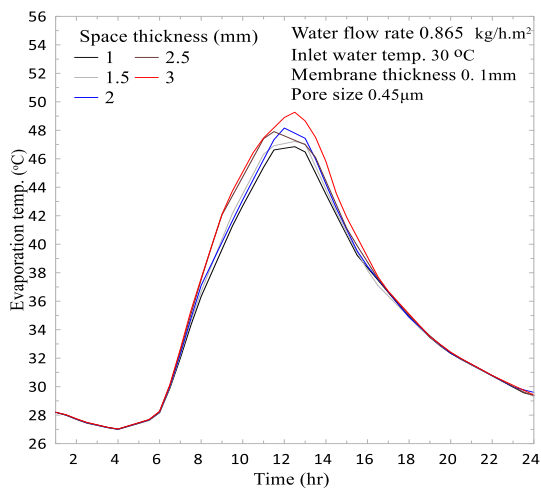
Figure 12. Effect of space thickness on the evaporation temperature.

A heat sink with a base thickness of 1 mm and five fins was attached to the last aluminum layer. The effect of fin height on the cell temperature is shown in Figure 16; the cell's temperature decreases with the increase in the fin's height due to the long fin's ability to dissipate heat more efficiently than the short fin. On the other hand, Figure 17 shows that increasing in the height of the fin reduced the water productivity due to the decrease in cell temperature. So, a trade-off should be made between the two cases. A fin height of 20 mm was chosen to achieve a lower cell temperature and more water productivity.
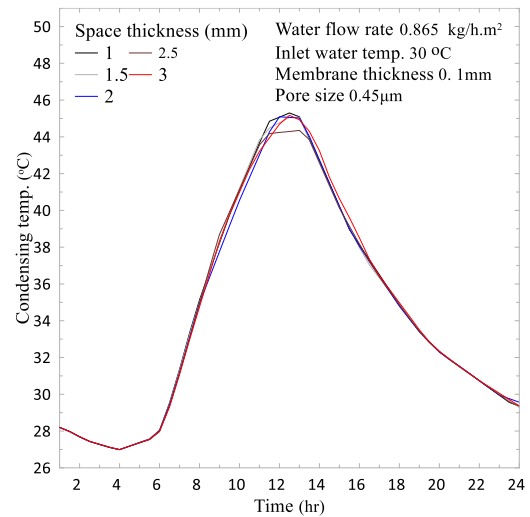
Figure 13. Effect of space thickness on the condensing temperature.
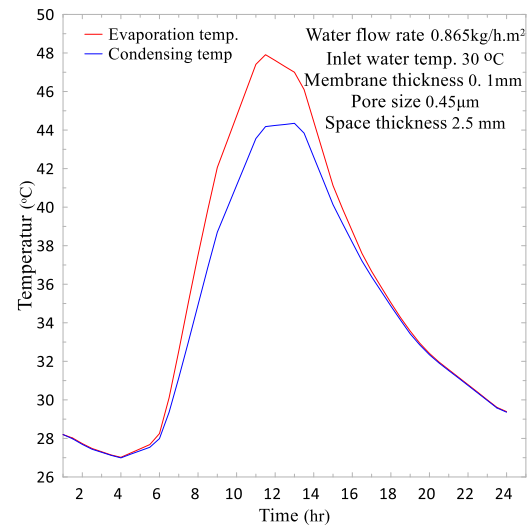
Figure 14. Difference between evaporation and condensing temperature at 2.5 mm space thickness.
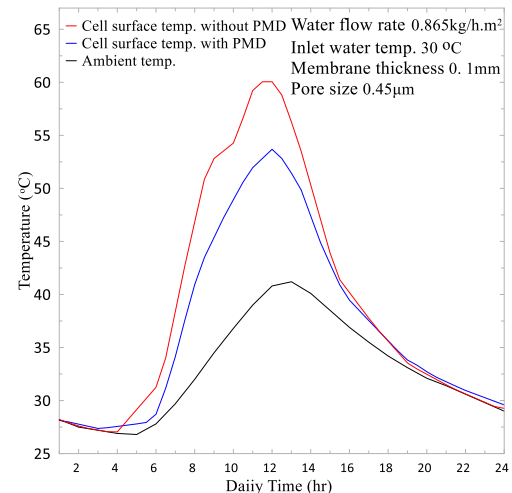
Figure 15. Effect of PMD on the cell surface temperature.

The increasing number of fins reduces the cell temperature, as shown in Figure 18. On the other hand, the water productivity decreases as the number of fins increases according to Figure 19. So, five fins were recommended for the economic point of view and the water productivity. The inlet temperature of the supply water, significantly, affects the cell surface temperature and water productivity, as shown in Figures 20 and 21. Figure 20 indicates that the cell surface temperature decreases as the inlet water temperature decreases. Figure 21 indicates that the low water temperature reduces the water productivity. In any case, the water temperature factor is difficult to control, as the water temperature depends on surrounding weather conditions.

Figure 22 shows the final parameter when the water temperature of inlet reached 30 °C, the space between evaporation and condensation was about of 2.5 mm, number of fins was 5 and the height of fins was 20mm in the 3-D plot for temperature distribution on the PMD.

Figure 19. Effect of the number of fins on the water productivity, fins height 2 cm.

Figure 16. Effect of fin height on the cell temperature.
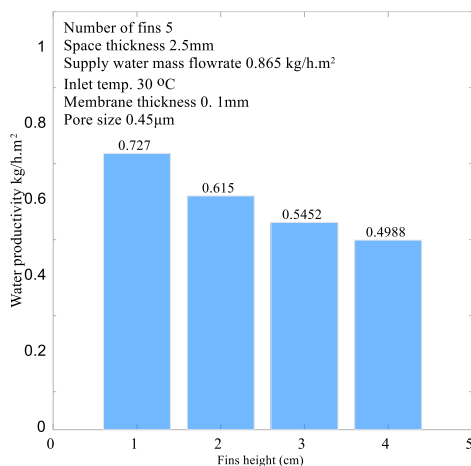
Figure 17. Effect of fin height on water productivity.
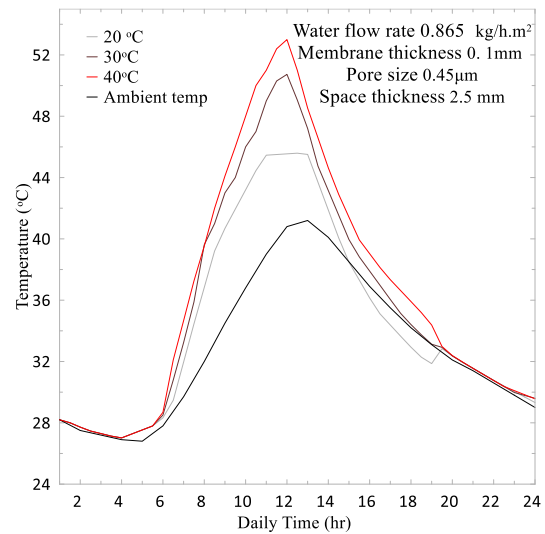
Figure 20. Effect of inlet water temperature on the cell surface temperature.

Figure 18. Effect of the number of fins on the cell surface temperature, fins height 20 mm.

Figure 21. Effect of inlet water temperature on water productivity.

height(3)=2 cm Time=12.5 h Surface: Temperature (degC)

Figure 22. 3-D plot for Temperature distribution on the PMD.

6. Conclusion

From current study, the main conclusions can be drawn as follows:

1. Adding the PMD system to the solar panel reduced the cell surface temperature by 7°C and produced a 0.727 kg/h.m^2 of freshwater.

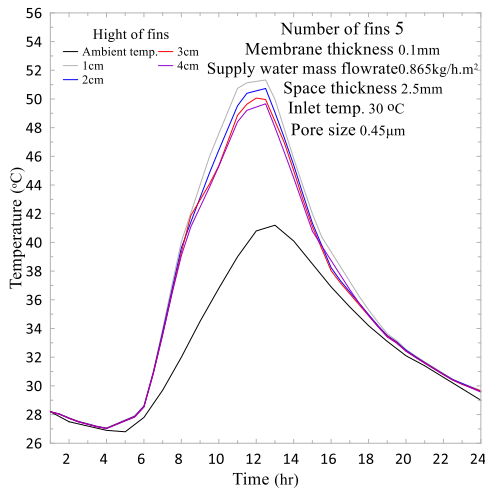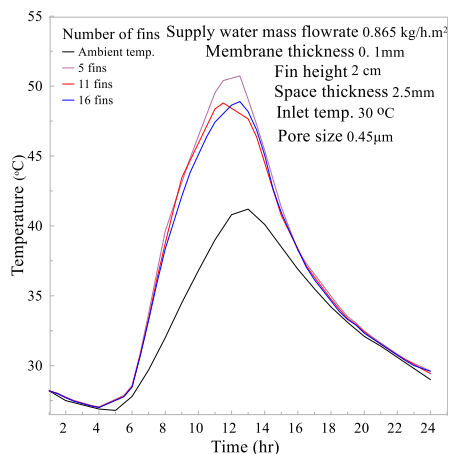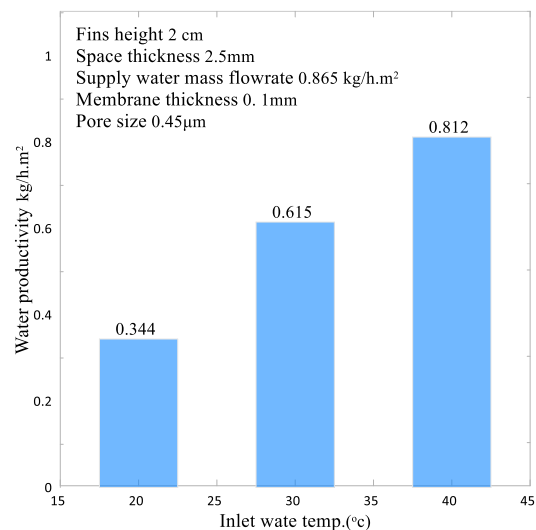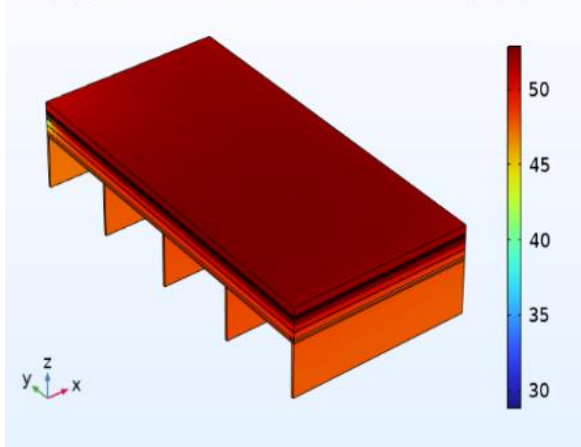2. The best membrane thickness was 100 μm, which gave the minimum temperature polarization and the maximum membrane coefficient.

3. The best space between the evaporation and condensation layer was 2.5 mm, which gave a temperature difference of 4°C between the evaporation and condensation layers.

4. Adding a heat sink of five fins with a fin height of 2 cm kept the maximum cell temperature at 50 and yielded water at about of 0.615 kg/h.m^2.

7. Nomenclature

c_p	Specific heat capacity (J/kg. K)	t	Time (sec)
c_m	membrane coefficient $(\frac{kg}{m^2 h\,Pa})$	Δp	The pressure difference (bar)
J	vapor flux (kg/m^{2}h)	u	Velocity in x-direction (m/sec)
dx	Elements in x_direction (m)	v	Velocity in y-direction (m/sec)
dy	Elements in y_direction (m)	w	Velocity in z-direction (m/sec)
dz	Elements in z_direction (m)		Greek Symbol
g	Gravity (m/sec^2)		
K_f	Thermalconductivity (W/m. K)	ϵ	Porosity of membrane
h	Heat transfer coffeient (W/m^{2}K)	ε	Pore size
pa	Pressure (bar)	μ	Dynamic viscosity (Pa.sec)
Q	Heat source (W/m^2)	ρ	Density (kg/m^3)
T	Temperature (k)	ω	pore tortuosity

References

[1] A. C. Lemay, S. Wagner, and B. P. Rand, "Current status and future potential of rooftop solar adoption in the United States," *Energy Policy*, vol. 177, pp. 113571, Jun. 2023, doi: 10.1016/J.ENPOL.2023.113571.

[2] M. Rabie, M. F. Elkady, and A. H. El-Shazly, "Hybrid membrane distillation/high concentrator photovoltaic system for freshwater production," *Energy Reports*, vol. 8, pp. 112–119, 2022, doi: 10.1016/j.egyr.2021.11.067.

[3] S. Aleid, "Design and Fabrication of Multi-functional Photovoltaic-Membrane Distillation Evaporative Crystallizer for Water Desalination, Electricity Generation, Salt Crystallization and Solar Cell Cooling " M.S. thesis, Dept. Sci. and Tech., Abdullah Univ., Thuwal, Kingdom of Saudi Arabia,2019.

[4] W.Wang, Y.Shi, C.Zhang, S.Hong, L. Shi, J. Chang, R. Li, Y.Jin, C. Ong, S. Zhuo, and P. Wang, "Simultaneous production of fresh water and electricity via multistage solar photovoltaic membrane distillation," *Nat. Commun.*, vol. 10, pp. 3012, Jul. 2019, doi: 10.1038/s41467-019-10817-6.

[5] Q. Zhao, H. Zhang, Z. Hu, and S. Hou, "A solar driven hybrid photovoltaic module/direct contact membrane distillation system for electricity generation and water desalination," *Energy Convers. Manag.*, vol. 221, pp. 113146,Oct.2020,doi:10.1016/j.enconman.2020.113146.

[6] U. Kumar, "Integration of Membrane Distillation and Solar Thermal Systems for Co-production of Purified Water and Heat" Ph.D. dissertation, Dept. Eng. Tech., KTH School of Industrial Engineering and Management., English, 2017.

[7] E. Chiavazzo, M. Morciano, F. Viglino, M. Fasano, and P. Asinari, "Passive solar high-yield seawater desalination by modular and low-cost distillation," *Nat. Sustain.*, vol. 1, no. 12, pp. 763–772, Dec. 2018, doi: 10.1038/s41893-018-0186-x.

[8] A. A. B. Baloch, H. M. S. Bahaidarah, P. Gandhidasan, and F. A. Al-Sulaiman, "Experimental and numerical performance analysis of a converging channel heat exchanger for PV cooling," *Energy Convers. Manag.*, vol. 103, pp. 14–27, Oct. 2015, doi: 10.1016/j.enconman.2015.06.018.

[9] C. G. Popovici, S. V. Hudişteanu, T. D. Mateescu, and N. C. Cherecheş, "Efficiency Improvement of Photovoltaic Panels by Using Air Cooled Heat Sinks," *Energy Procedia*, vol. 85, pp. 425–432, Jan. 2016, doi: 10.1016/j.egypro.2015.12.223.

[10] G. Li and L. Lu, "Modeling and performance analysis of a fully solar-powered stand-alone sweeping gas membrane distillation desalination system for island and coastal households," *Energy Convers. Manag.*, vol. 205, pp. 112375, Feb. 2020, doi: 10.1016/j.enconman.2019.112375.

[11] W. Wang, "The Design and Fabrication of the Multistage-Membrane Distillation Device Integrated with Solar Cell for Simultaneous Water and Electricity Production via Sunlight Dissertation" Ph.D. dissertation, Dept Sci. and Tech., Abdullah Univ., Thuwal, Kingdom of Saudi Arabia,2020.

[12] W. Z. Leow, Y. M. Irwan, I. Safwati, M. Irwanto, A. R. Amelia, Z. Syafiqah, M. I. Fahmi and N. Rosle, "Simulation study on photovoltaic panel temperature under different solar radiation using computational fluid

dynamic method," *J. Phys. Conf. Ser. 1432 012052, Malaysia*, Jan. 2020, vol. 1432, pp. 012052, doi: 10.1088/1742-6596/1432/1/012052.

[13] J. M. Smith, *Introduction to chemical engineering thermodynamics*,6nd Ed.New York: McGraw-Hill,1950.

[14] T. L. Bergman, A. S. Lavine, F. P. Incropera, and D. P. DeWitt, "Fundamental of Heat and Mass Transfer," in *Fluid Mech. its Appl.*,8nd ed. New York: McGraw-Hill, 2011, pp. 321–338. [Online]. Available: https://www.wiley.com/en-us/Fundamentals+of+Heat+and+Mass+Transfer%2C+8th+Edition-p-9781119353881,(Accessed Mar. 04, 2023).

[15] M.D.Koretsky, *Engineering and Chemical Thermodynamics*, 2nd Ed.New York: Wiley, 2012.

[16] A. O. Imdakm and T. Matsuura, "A Monte Carlo simulation model for membrane distillation processes: Direct contact (MD)," *J. Memb. Sci.*, vol. 237, pp. 51–59, Jul. 2004, doi:10.1016/j.memsci.2004.03.005.

[17] S. Srisurichan, R. Jiraratananon, and A. G. Fane, "Mass transfer mechanisms and transport resistances in direct contact membrane distillation process," *J. Memb. Sci.*, vol. 277, pp.186–194, Jun.2006, doi: 10.1016/j.memsci.2005.10.028.

[18] N. Nishiyama and T. Yokoyama, "Permeability of porous media: Role of the critical pore size," *J. Geophys. Res. Solid Earth*, vol. 122,pp. 6955–6971, Aug.2017, doi: 10.1002/2016JB013793.

[19] W. Wang, S. Aleid, Y. Shi, C. Zhang, R. Li, M. Wu, S. Zhu, and P.Wang "Integrated solar-driven PV cooling and seawater desalination with zero liquid discharge," *Joule*, vol. 5, pp. 1873–1887, Jul. 2021, doi: 10.1016/j.joule.2021.05.010.

Research Article

Thermodynamic Optimization and Energy-Exergy Analyses of the Turboshaft Helicopter Engine

[1]M. Siyahi [ID], [2]*H. Siyahi [ID], [3]M. Fallah [ID], [4]Z. Mohammadi [ID]

[1,2] Department of Aeronautical Engineering, Istanbul Technical University -Turkey
[3,4] Mechanical Engineering Department, Azarbaijan Shahid Madani University -Iran
E-mails: [1]siyahi20@itu.edu.tr, [2]*siyahi16@itu.edu.tr, [3]mfallah@azaruniv.ac.ir, [4]zahra_mohammadij@yahoo.com

Abstract

Energy demand is a critical contemporary concern, with significant implications for the future. While exploring renewable or sustainable energy sources offers potential solutions, optimizing energy consumption in existing power generation systems is also key. Aviation accounts for a substantial portion of energy demand, underscoring the importance of energy efficiency in this sector. Conventional energy analyses may be misleading; hence, employing exergy-based analyses provides a clearer understanding of energy consumption. Also, most of these analyses do not include the effect of the turbine blade's cooling in calculations. In the present study, exergy analyses have been conducted on a helicopter turboshaft engine with turbine-blades cooling, focusing on design parameters such as ambient temperature, compressor pressure ratio, and turbine inlet temperature. Thermodynamic optimizations are conducted using a genetic algorithm. Results show that increasing pressure ratio and turbine inlet temperature boost performance, yet technical restrictions on compressor and turbine size, and metallurgical constraints on turbine blades' material limit these gains. Sea level scenario prioritizes ambient temperature-drop for enhancing net-work and efficiency, while altitude-gain boosts turboshaft performance. Combustion chambers incur the highest exergy destruction of 74-80%, followed by 16-20% and 4-6% exergy destructions in the turbine and compressor, respectively. Lower air temperatures and higher flight altitudes demand larger fuel consumption for equivalent turbine inlet temperature, albeit enhancing cooling capacity and reducing required cooling air fraction for turbine blades.

Keywords: Turboshaft engine; energy-exergy analyses; thermodynamic optimization; energy efficiency; exergy efficiency; exergy destruction.

1. Introduction

A turboshaft engine is an engine type that is designed to generate shaft power rather than jet thrust. This type of engine is widely used for applications that require large power with a lightweight and small size. Turboshaft engines are widely used in helicopters, hovercrafts, tanks, boats, and ships [1, 2]. Because of the huge usage of turboshaft engines in helicopters, it worth paying special attention to the performance analysis of this engine type via energy efficiency and optimization [3-5]. Energy can be explained in two parts, exergy is the maximum accessible work or potential work and anergy is a part that cannot be benefited from. In other words, exergy is the quality of energy and can be expressed as how good we are or can be using an energy source. Exergy analysis is a practical and powerful tool for performance analysis [6]. Many engineers and scientists suggest that exergy analysis is a highly effective method for evaluating and enhancing thermodynamic performance, and is superior to energy analysis [7]. Many researchers have investigated aircraft engines and propulsion systems using exergy analysis [8-17]. Others examine the importance of defining a reference environment that varies with altitude and applying that work to a turbojet engine [18, 19]. Many have applied parametric studies based on different ambient and operating parameters along with exergy methods to

analyze the performance of an aircraft engine [20-22]. Besides, the parametric studies can give a good understanding of the performance change of aircraft engines in different ambient and design situations. The other research explains that the ambient air pressure and temperature, compressor pressure ratio, turbine inlet temperature, and the efficiency of components are the most important parameters that influence the performance of the gas turbine cycle [23]. Recent studies have applied the exergy analysis to optimize the performance of aircraft propulsion systems [24]. While some studies address the optimization of the cruise velocity of an aircraft [3], others investigate the engine configuration optimization methods [25]. One of the most beneficial impacts of exergy analysis is that it can be utilized for economic assessments [26]. They develop several parameters such as thrust cost rate, cost of exergy destruction, relative cost difference, and exergoeconomic cost to calculate the thrust cost rate. Moreover, exergy analyses can be a useful tool for studying environmental effects [27]. The authors of the present study have noticed that there is a gap in the literature studying turboshaft engines from the 2nd law of thermodynamics point of view which includes turbine cooling. The main focus of the present research work is on the parametric study, exergy analysis, and thermodynamic optimization of a turboshaft helicopter

engine equipped with a practical model for turbine blades' cooling.

2. Governing Equations

All explanations for energy and exergy analyses are explained in detail in Appendix A and Appendix B. Noticing that 1, 2, 3, and 4 states respectively introduce the compressor inlet, combustion chamber inlet (compressor outlet), turbine inlet (combustion chamber outlet), and exhaust (turbine outlet) in Figure 1, the simplified equations for thermodynamic analyses of different components of the turboshaft engine are revealed in the following sections.
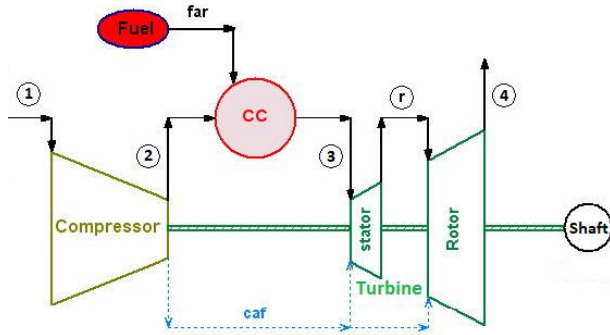

Figure 1. Schematic of turboshaft-engine configuration.

2.1 Polytropic Compressor

Considering the definition of the compressor's polytropic efficiency, it can be written as [28-32]:

$$\eta_{poly,comp} = \frac{\bar{R}T\frac{dP}{P}}{\overline{C}_{p,air}dT} \tag{1}$$

which the molar specific heat coefficient of air at constant pressure based on its elements is [33-38]:

$$\overline{C}_{p,air} = \frac{\Sigma(n_i\overline{C}_{p,i})_{air}}{\Sigma(n_i)_{air}} \tag{2}$$

By integrating equation (1) the compressor outlet temperature (COT=T2) can be calculated as:

$$\int_{T_1}^{T_2} \overline{C}_{p,air} \frac{dT}{T} = \int_{P_1}^{P_2} \frac{\bar{R}}{\eta_{poly,comp}} \frac{dP}{P} \tag{3}$$

Mass conservation for compressor, [33-38] is:

$$\dot{m}_1 = \dot{m}_2 + (caf)\dot{m}_1 \tag{4}$$

Energy conservation for compressor, [33-38] is:

$$\dot{W}_{comp} + \dot{m}_1 e_1 = \dot{m}_1 e_2 \tag{5}$$

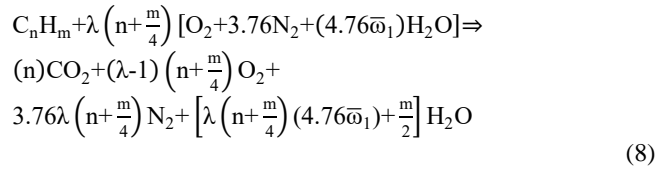The exergy balance for the compressor can be written as, [33-38]:

$$\dot{W}_{comp} + \dot{m}_1 ex_1 = \dot{m}_1 ex_2 + \dot{Ex}_{D,comp} \tag{6}$$

The exergy efficiency of the compressor is [33-38]:

$$\eta_{II,comp} = \frac{(\dot{W}_{comp} - \dot{Ex}_{D,comp})}{\dot{W}_{comp}} 100 \tag{7}$$

2.2 Combustion Chamber

After the compressor, air enters the combustion chamber as an oxidizer with a molar ratio of 21% oxygen and 79% nitrogen. The combustion process is carried out assuming that nitrogen does not participate in the reaction. The reaction equation considering the factor of excess air (λ) can be calculated as, [28-32]:

$$C_nH_m + \lambda\left(n+\frac{m}{4}\right)[O_2 + 3.76N_2 + (4.76\overline{\omega}_1)H_2O] \Rightarrow$$
$$(n)CO_2 + (\lambda-1)\left(n+\frac{m}{4}\right)O_2 +$$
$$3.76\lambda\left(n+\frac{m}{4}\right)N_2 + \left[\lambda\left(n+\frac{m}{4}\right)(4.76\overline{\omega}_1) + \frac{m}{2}\right]H_2O \tag{8}$$

with the assumption of an adiabatic combustion process, the energy conservation for the combustion process is as follows [28-32]:

$$\Sigma(n_i\overline{h}_i)_{Reactants} = \Sigma(n_i\overline{h}_i)_{Products} \tag{9}$$

which the enthalpy of ith element $(\overline{h}_i)$ is:

$$\overline{h}_i = \overline{h}_f^0 + \int_{298.15}^T \overline{C}_p dT \tag{10}$$

The energy equation of combustion can be rewritten as:

$$\int_{298.15}^{T_f} \overline{C}_{p,C_nH_m}dT + \lambda\left(n+\frac{m}{4}\right)\int_{298.15}^{T_2} \overline{C}_{p,O_2}dT +$$
$$\lambda\left(n+\frac{m}{4}\right)3.76\int_{298.15}^{T_2} \overline{C}_{p,N_2}dT +$$
$$\lambda\left(n+\frac{m}{4}\right)4.76\overline{\omega}_1\int_{298.15}^{T_2} \overline{C}_{p,H_2O}dT =$$
$$n\int_{298.15}^{TIT} \overline{C}_{p,CO_2}dT + (\lambda-1)\left(n+\frac{m}{4}\right)\int_{298.15}^{TIT} \overline{C}_{p,O_2}dT +$$
$$3.76\lambda\left(n+\frac{m}{4}\right)\int_{298.15}^{TIT} \overline{C}_{p,N_2}dT +$$
$$\left[\lambda\left(n+\frac{m}{4}\right)(4.76\overline{\omega}_1) + \frac{m}{2}\right]\int_{298.15}^{TIT} \overline{C}_{p,H_2O}dT \tag{11}$$

alternatively, by knowing the turbine inlet temperature (TIT) and solving energy conservation for combustion chamber the excess air (λ) is calculated. Consequently, by knowing the λ and the efficiency of the combustion chamber ($\eta_{I,cc}$), the fuel-air ratio (far) is calculated as:

$$far = \frac{M_{C_nH_m}}{\lambda\left(n+\frac{m}{4}\right)4.76(1+\overline{\omega}_1)M_{air}\eta_{I,cc}}(1-caf) \tag{12}$$

Mass conservation for combustion chamber [33-38]:

$$\dot{m}_2 + \dot{m}_f = \dot{m}_3 \tag{13}$$

which fuel mass $(\dot{m}_f)$ equals:

$$\dot{m}_f = (far)\dot{m}_1 \tag{14}$$

The exergy balance for the combustion chamber is given as [33-38]:

$$\dot{m}_2 ex_2 + \dot{m}_f ex_f = \dot{m}_3 ex_3 + \dot{Ex}_{D,cc} \tag{15}$$

and the exergy efficiency for combustion can be written as [33-38]:

$$\eta_{II,cc} = \left[1 - \frac{\dot{Ex}_{D,cc}}{(far)\dot{m}_1 ex_f}\right]100 \tag{16}$$

2.3 Cooling Air Fraction (caf) of Turbine Blades

To simulate the turboshaft engine more realistically, it is assumed that turbine has one stationary and one rotary stage and a cooling method that gives a simple relationship between turbine inlet temperature (TIT) and the rotor inlet temperature (T_r) is applied for turbine blades as [39-41]:

$$T_r = 0.8451(TIT) + 136.2 \tag{17}$$

which the temperatures are in degrees Celsius.

Mass conservation for stationery blades stage is as:

$$\dot{m}_3 + \left(\frac{caf}{2}\right)\dot{m}_1 = \dot{m}_r \tag{18}$$

replacing equation 13 in equation 18, $\dot{m}_r$ can be rewritten as:

$$\dot{m}_r = \left(1 - \frac{caf}{2} + far\right)\dot{m}_1 \tag{19}$$

Energy conservation for stationary blades is:

$$\dot{m}_3 e_3 + \left(\frac{caf}{2}\right)\dot{m}_1 e_2 = \dot{m}_r e_r \tag{20}$$

by replacing equations 13 and 19 in equation 20 the energy equation will be as:

$$(1 - caf + far)\dot{m}_1 e_3 + \left(\frac{caf}{2}\right)\dot{m}_1 e_2 = \left(1 - \frac{caf}{2} + far\right)\dot{m}_1 e_r \tag{21}$$

after simplification, the cooling air fraction (caf) can be calculated as:

$$caf = \frac{2(1 + far)(e_3 - e_r)}{(2e_3 - e_2 - e_r)} \tag{22}$$

2.4 Polytropic Turbine

Considering the definition of the turbine's polytropic efficiency, it can be written as [28-32]:

$$\eta_{poly,turb} = \frac{\overline{C}_{p,g}dT}{\overline{R}T\frac{dP}{P}} \tag{23}$$

which the molar specific heat coefficient of products at constant pressure based on its elements is [33-38]:

$$\overline{C}_{p,g} = \frac{\Sigma(n_i \overline{C}_{p,i})_{product}}{\Sigma(n_i)_{product}} \tag{24}$$

By integrating equation (23) the turbine outlet temperature ($TOT = T_4$) can be calculated as:

$$\int_{T_r}^{TOT} \overline{C}_{p,g}\frac{dT}{T} = \int_{P_3}^{P_4} \eta_{poly,turb}\overline{R}\frac{dP}{P} \tag{25}$$

Mass conservation for turbine is [33-38]:

$$\dot{m}_3 + (caf)\dot{m}_1 = \dot{m}_4 \tag{26}$$

The Energy conservation for turbine is [33-38]:

$$\dot{m}_3 e_3 + (caf)\dot{m}_1 e_2 = \dot{m}_4 e_4 + \dot{W}_{turb} \tag{27}$$

The exergy balance equation for the turbine can be written as [33-38]:

$$\dot{m}_3 ex_3 + (caf)\dot{m}_1 ex_2 = \dot{m}_4 ex_4 + \dot{W}_{turb} + \dot{Ex}_{D,turb} \tag{28}$$

The exergy efficiency of the turbine is as [33-38]:

$$\eta_{II,turb} = \frac{\dot{W}_{turb}}{(\dot{W}_{turb} + \dot{Ex}_{D,turb})}100 \tag{29}$$

2.5 Energy-Exergy Analysis of the Entire Cycle

Considering the special mechanical efficiency (η_{mech}), the cycle net work is [33-38]:

$$\dot{W}_{net} = (\dot{W}_{turb} - \dot{W}_{comp})\eta_{mech} \tag{30}$$

By using the low heat value (LHV) of the fuel, the thermal efficiency of the cycle (energy efficiency) can be expressed as follows [33-38]:

$$\eta_{I,cycle} = \frac{\dot{W}_{net}}{(far)\dot{m}_1\,LHV}100 \tag{31}$$

According to the equations mentioned in the previous sections and chapter, the exergy balance for the entire gas turbine cycle can be written as follows, [33-38]:

$$\dot{m}_1 ex_1 + \dot{m}_f ex_f = \dot{m}_4 ex_4 + \dot{W}_{net} + \dot{Ex}_{D,cycle} \tag{32}$$

The irreversibility of the entire system can be considered as the summation of the exergy destructions of individual components of the cycle [33-38]:

$$\dot{I}_{D,cycle} = \dot{Ex}_{D,cycle} = \dot{Ex}_{D,comp} + \dot{Ex}_{D,cc} + \dot{Ex}_{D,turb} \tag{33}$$

Finally, the exergy efficiency of entire cycle can be obtained as [33-38]:

$$\eta_{II,cycle} = \frac{\dot{W}_{net}}{(far)\dot{m}_1\,ex_f}100 \tag{34}$$

All required equations for the energy-exergy analyses and thermodynamic optimization of the turboshaft engine have been summarized in Appendix C.

3. Mathematical Method

The genetic method is a robust optimization algorithm that is designed to reliably locate a global optimum even in the presence of local optima. The genetic method implemented in the engineering equation solver (EES) program is derived from the public domain Pikaia optimization program (version 1.2) written by Paul Charbonneau and Barry Knapp at the National Center for Atmospheric Research (NCAR). A detailed explanation of genetic optimization algorithms in general and specific details of the Pikaia program are provided in [42].

The genetic method intends to mimic the processes occurring in biological evolution. A population of individuals (sample points) is initially chosen at random from the range specified by the bounds of the independent variables. The individuals in this population are surveyed to determine their fitness (the values of the objective function as quantified by the value of the variable that is to be minimized or maximized). Then a new generation of individuals is generated in a stochastic manner by 'breeding' selected members of the current population. The characteristics of an individual that are passed on to the next generation are represented by encoded values of its independent variables. The probability that an individual in the current population will be selected for breeding the next generation is an increasing function of its fitness. The

'breeding' combines the characteristics of two parents in a stochastic manner. Additional random variations are introduced by the possibility of 'mutations' for which the offspring may have characteristics that differ markedly from those of the parents. In the current implementation, the number of individuals in the population remains constant for each generation.

The three parameters in the genetic method that are most responsible for identifying an optimum and for the associated computing effort are the number of individuals in a population, the number of generations to explore, and the maximum mutation rate.

Unlike the Conjugate Directions and Variable Metric methods, the genetic method is not affected by the guess values of the independent parameters. However, the lower and upper bounds on the independent parameters are extremely important since the initial population and subsequent stochastic selections are chosen from within these bounds.

4. Results

In the present study, the performance analyses of a turboshaft engine cycle equipped with turbine blades' cooling are carried out via the engineering equation solver (EES) program.

The energy-exergy analyses have been done with the parametric studies of turboshaft engine's specific net-work (w_{net}), energy efficiency (η_I), and exergy efficiency (η_{II}) with respect to different ambient conditions and different operating conditions. The metallurgical and technological considerations limit the maximum turbine inlet temperature and pressure ratio of the TIT=1200°C and r_p=35 for the turboshaft engines.

A typical maximum flight altitude of 9 km has been specified for the helicopter engine.

The thermodynamic optimizations have been performed through maximization of w_{net}, η_I and η_{II} by using the genetic algorithm technique.

The fuel used in turboshaft engine is "Kerosene or Dodecane" with the chemical formula of $C_{12}H_{26}$ which is considered to be the most common fuel used in today's jet engines.

It is assumed that turboshaft engine works at steady state steady flow (SSSF) condition.

4. 1 Validation

A program has been written for an open simple gas turbine cycle and results have been compared with reference data [23] in Table 1.

Table 1. The Validation Table of EES Program Results vs. Results of Reference, [23].

Variables	Reference	Present Study	Deviation
T_{amb}	15 °C	15 °C	**0.0 %**
P_{amb}	101 kPa	100 kPa	**0.1 %**
RH_{amb}	60 %	60 %	**0.0 %**
$\eta_{poly,comp}$	92 %	92 %	**0.0 %**
$\eta_{poly,turb}$	86 %	89 %	**3.5 %**
η_{mech}	99.5 %	100 %	**0.5 %**
$r_{p,comp}$	20	20	**0.0 %**
COT	449.6 °C	438.6 °C	**2.4 %**
TIT	1331.3 °C	1330 °C	**0.1 %**
TOT	620 °C	617.1 °C	**0.5 %**
$\eta_{I,cycle}=\eta_{thermal,cycle}$	40.16 %	40.08 %	**0.2 %**

It could be clearly figured out that the maximum deviation of the calculated results is 3.5%, which is reasonable for a parametric study.

4. 2 Turboshaft Engine

It is assumed that ambient relative humidity (RH_{amb}=15%) and operating turbine inlet temperature (TIT=1200 °C) are constant for all cycles. The thermodynamics optimization and energy-exergy analyses have been done for a turboshaft engine in different air temperatures and altitudes.

At sea level, results show that decreasing the temperature of air leads to an increase in the density. Since a compressor works with the same volumetric flow rate, by increasing the air density, the inlet air mass flow rate increases. Moreover, the fuel-air ratio increases to reach the same turbine inlet temperature, consequently, the entire cycle mass flow rate increases. Therefore, for the same turbine inlet temperature decrease at the compressor inlet temperature will increase the specific net-work of the turboshaft engine (Table 2).

Table 2. Optimization of the Performance of the Turboshaft Engine Cycle for the Maximum Specific Work (w_{net}) at Sea Level, RH_{amb}=15%, TIT=1200 °C and Different Ambient Temperatures.

T_{amb} [°C]	TIT [°C]	Design Parameters	Values
10	1200	$r_{p.comp}$	18.13
		far [kg/kg]	0.01936
		caf [kg/kg]	0.1285
		λ (excess air fraction)	3.052
		$\boldsymbol{w_{net,max}}$ **[kJ/kg]**	**341.8**
25	1200	$r_{p.comp}$	16.46
		far [kg/kg]	0.01903
		caf [kg/kg]	0.1303
		λ (excess air fraction)	3.093
		$\boldsymbol{w_{net,max}}$ **[kJ/kg]**	**321.6**
40	1200	$r_{p.comp}$	16.46
		far [kg/kg]	0.01829
		caf [kg/kg]	0.1347
		λ (excess air fraction)	3.187
		$\boldsymbol{w_{net,max}}$ **[kJ/kg]**	**303**

Table 3. Optimization of the Performance of the Turboshaft Engine Cycle for the Maximum Thermal Efficiency ($\eta_{I,cycle,max}$) at Sea Level, RH_{amb}=15%, TIT=1200 °C and Different Ambient Temperatures.

T_{amb} [°C]	TIT [°C]	Design Parameters	Values
10	1200	$r_{p.comp}$	34.99
		far [kg/kg]	0.01596
		caf [kg/kg]	0.149
		λ (excess air fraction)	3.614
		$\boldsymbol{\eta_{I,cycle,max}}$	**46.68**
25	1200	$r_{p.comp}$	34.99
		far [kg/kg]	0.01499
		caf [kg/kg]	0.1563
		λ (excess air fraction)	3.806
		$\boldsymbol{\eta_{I,cycle,max}}$	**45.42**
40	1200	$r_{p.comp}$	34.99
		far [kg/kg]	0.01408
		caf [kg/kg]	0.1643
		λ (excess air fraction)	3.999
		$\boldsymbol{\eta_{I,cycle,max}}$	**43.98**

T_{amb} [℃]	TIT [℃]	Design Parameters	Values
10	1200	$r_{p.comp}$	34.99
		far [kg/kg]	0.01596
		caf [kg/kg]	0.149
		λ (excess air fraction)	3.614
		$\eta_{II,cycle,max}$	**42.52**
25	1200	$r_{p.comp}$	34.99
		far [kg/kg]	0.01499
		caf [kg/kg]	0.1563
		λ (excess air fraction)	3.806
		$\eta_{II,cycle,max}$	**41.37**
40	1200	$r_{p.comp}$	34.99
		far [kg/kg]	0.01408
		caf [kg/kg]	0.1643
		λ (excess air fraction)	3.999
		$\eta_{II,cycle,max}$	**40.06**

Tables 3 and 4 show that both energy and exergy efficiencies will significantly increase with a decrease in air temperature because of the performance improvement of the compressor and entire cycle at lower inlet temperatures.
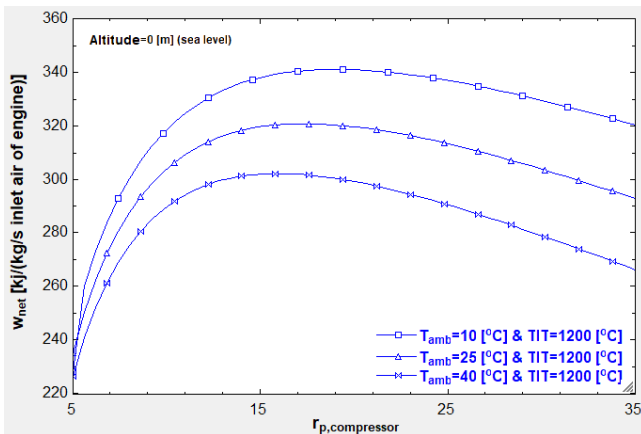

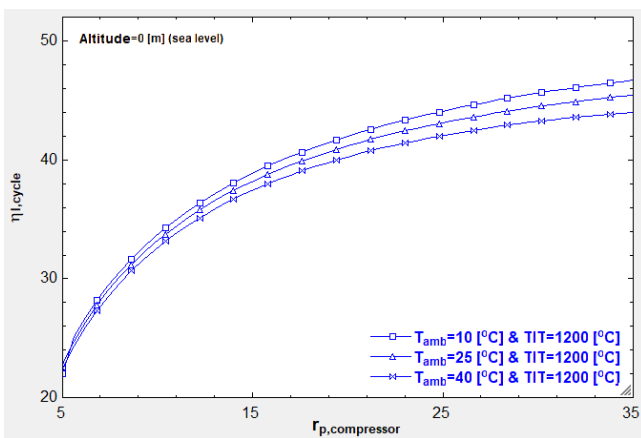Figure 2. Change curve of w_{net} vs. $r_{p,comp}$ at sea level, $RH_{amb}=15\%$, TIT =1200 ℃ and different ambient temperatures for turboshaft engine.

Figure 3. Change curve of thermal efficiency ($\eta_{I,cycle}$) vs. $r_{p,comp}$ at sea level, $RH_{amb}=15\%$, TIT=1200 ℃ and different ambient temperatures for turboshaft engine.

In Figures 2, 3, and 4 the curves of different performance parameters of the turboshaft engine have been plotted versus

changes of pressure ratio ($r_{p,comp}$). Results show that specific net-work (w_{net}), energy efficiency ($\eta_{I,cycle}$) and exergy efficiency ($\eta_{II,cycle}$) bear an indirect relationship with ambient temperature. Moreover, there is an optimum pressure ratio for the maximum net work because at the lower r_p the compressor work is small in comparison with the turbine work but as the r_p increases the slop of required compressor work exceeds the slop of work production by the turbine. The maximum w_{net} occurs around $r_{p,comp}$=17-18 (Figure 2), while $\eta_{I,cycle}$ and $\eta_{II,cycle}$ continuously increase for larger pressure ratios (Figures 3,4).
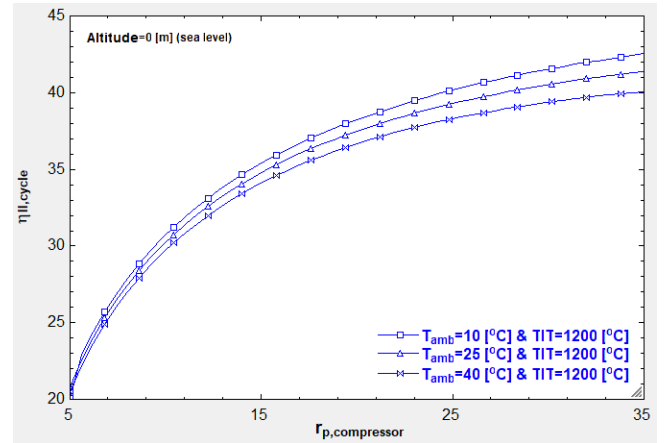
Figure 4. Change curve of exergy efficiency ($\eta_{II,cycle}$) vs. $r_{p,comp}$ at sea level, $RH_{amb}=15\%$, TIT=1200 ℃ and different ambient temperatures for turboshaft engine.
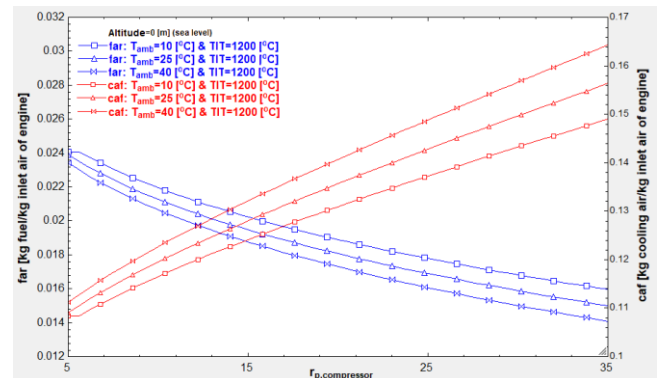
Figure 5. Change curves of caf and far vs. $r_{p,comp}$ at sea level, $RH_{amb}=15\%$, TIT=1200 ℃ and different ambient temperatures for turboshaft engine.
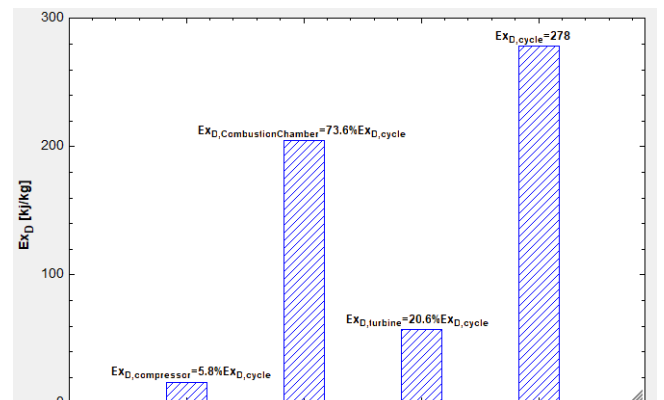
Figure 6. Bar plot of exergy destructions (Ex_D) of components at sea level, Tamb=25 ℃, RHamb=15%, TIT=1200 ℃ and $\eta_{II,max}$=41.37 for turboshaft engine.

Results also show that at sea level to obtain the same turbine inlet temperature (TIT), the fuel consumption (far) is increases by decreasing of the air temperatures. On the contrary, the decrease of air temperature enlarges the cooling capacity, consequently, the amount of required cooling air fraction (caf) for turbine blades decreases (Figure 5).

Figure 6 shows that in optimum exergy efficiency of the cycle the highest amount of exergy destruction (Ex_D) belongs to the combustion chamber (73%), followed by the turbine (21%) and compressor (6%).

Predictably, the highest amount of η_{II} belongs to the compressor (97%), followed by the turbine (94%) and combustion chamber (71%) as shown in Figure 7.
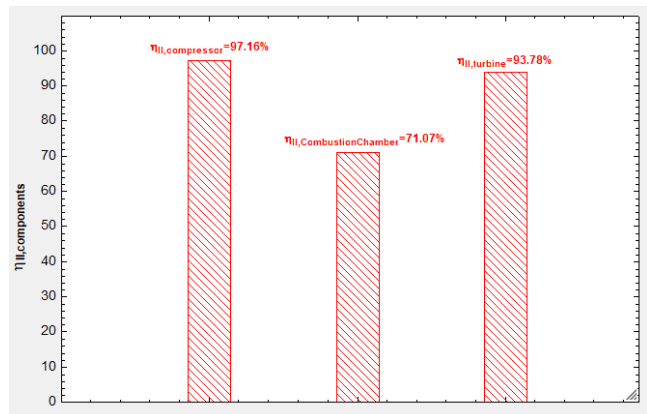
Figure 7. Bar plot of exergy efficiency (η_{II}) of components at sea level, RH_{amb}=15%, T_{amb} =25 °C, TIT=1200 °C and $\eta_{II,max}$=41.37 for turboshaft engine.

In the following part, the performance analyses of turboshaft have been studied at different altitudes.

At different altitudes, both ambient air temperature and density play important roles in determining the performance of turboshaft engines. Knowing that specific altitude is accompanied by specific temperature and density, the performance has been calculated for different altitudes. By increasing the flight altitude from 6 km to 9 km, both the air temperature and density decreased (Table 5).

Table 5. Ambient air properties at different altitudes.

Altitude [m]	T_{amb} [°C]	P_{amb} [kPa]	ρ_{amb} [kg/m^3]
6000	-24.0	47.18	0.6597
9000	-43.5	30.74	0.4664

Table 6. Optimization of the Performance of the Turboshaft Engine Cycle for the Maximum Specific Work (w_{net}) at TIT=1200 °C and Different Altitudes.

Altitude [m]	TIT [°C]	Design Parameters	Values
6000	1200	$r_{p.comp}$	22.51
		far [kg/kg]	0.02032
		caf [kg/kg]	0.1238
		λ (excess air fraction)	2.926
		$w_{net,max}$ **[kJ/kg]**	**392.7**
9000	1200	$r_{p.comp}$	26.25
		far [kg/kg]	0.02085
		caf [kg/kg]	0.1214
		λ (excess air fraction)	2.86
		$w_{net,max}$ **[kJ/kg]**	**425.9**

The air temperature drop increases the required fuel mass to achieve the same turbine inlet temperature. On the other hand, decreasing the density of air decreases the inlet mass

flow rate. The temperature drop with altitude-gain plays a dominant role rather than the density drop in the change of total mass flow rate. Consequently, the entire mass flow rate will increase with higher altitudes and lead to an increase in the specific net-work of the turboshaft (Table 6).

The results show that both energy and exergy efficiencies are slightly increasing with altitude gain (Tables 7 and 8).

Table 7. Optimization of the Performance of the Turboshaft Engine Cycle for the Maximum Thermal Efficiency ($\eta_{I,cycle,max}$) at TIT=1200 °C and Different Altitudes.

Altitude [m]	TIT [°C]	Design Parameters	Values
6000	1200	$r_{p.comp}$	34.99
		far [kg/kg]	0.01823
		caf [kg/kg]	0.1346
		λ (excess air fraction)	3.22
		$\eta_{I,cycle,max}$	**49.6**
9000	1200	$r_{p.comp}$	34.99
		far [kg/kg]	0.01956
		caf [kg/kg]	0.1276
		λ (excess air fraction)	3.027
		$\eta_{I,cycle,max}$	**50.2**

Table 8. Optimization of the Performance of the Turboshaft Engine Cycle for the Maximum Exergy Efficiency ($\eta_{II,cycle,max}$) at TIT=1200 °C and Different Altitudes.

Altitude [m]	TIT °C	Design Parameters	Values
6000	1200	$r_{p.comp}$	34.99
		far [kg/kg]	0.01823
		caf [kg/kg]	0.1346
		λ (excess air fraction)	3.22
		$\eta_{II,cycle,max}$	**44.69**
9000	1200	$r_{p.comp}$	34.99
		far [kg/kg]	0.01956
		caf [kg/kg]	0.1276
		λ (excess air fraction)	3.027
		$\eta_{II,cycle,max}$	**45.73**

Figures 8, 9, and 10 show that the performance values of turboshaft engine of w_{net}, $\eta_{I,cycle}$ and $\eta_{II,cycle}$ increase with altitude gain from 6 km to 9 km.

The maximum w_{net} for 6 km and 9 km altitudes occurs at $r_{p,comp}$=22.5 and 26.2, respectively (Figures 8, 9), while $\eta_{I,cycle}$ and $\eta_{II,cycle}$ continuously increase for larger pressure ratios (Figure 10).

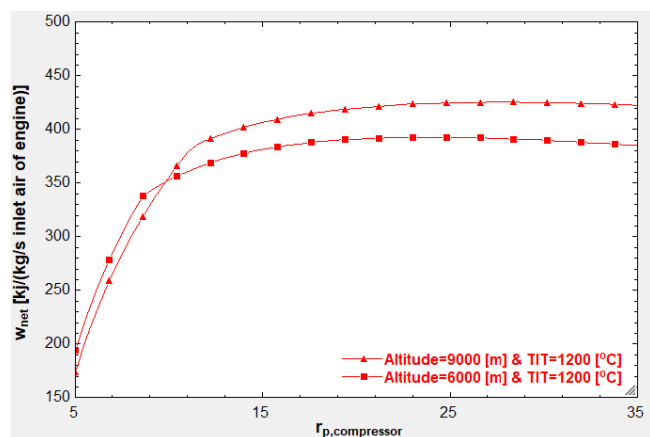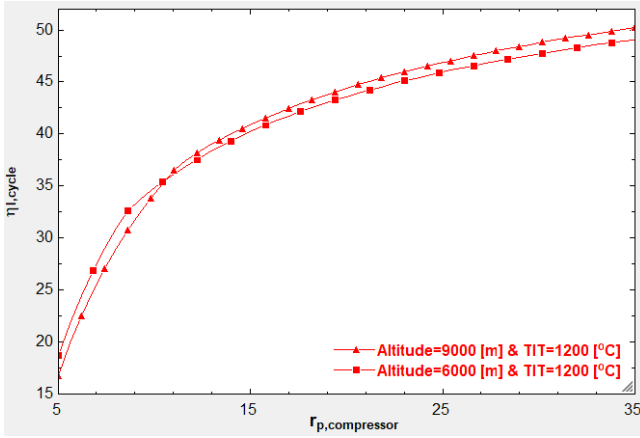*Figure 8. Change curve of w_{net} vs. $r_{p,comp}$ at TIT=1200 °C and different altitudes for turboshaft engine.*

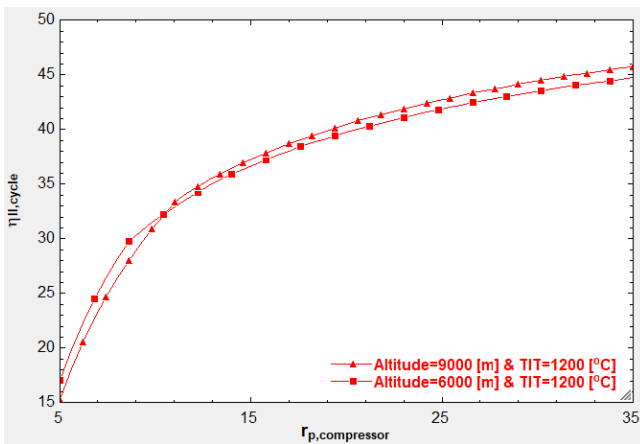*Figure 9. Change curve of thermal efficiency ($\eta_{I,cycle}$) at TIT=1200 °C and different altitudes for turboshaft engine.*

Figure 10. Change curve of exergy efficiency ($\eta_{II,cycle}$) at TIT=1200 °C and different altitudes for turboshaft engine.

Knowing that ambient temperature and density bear different influences on the fuel consumption and cooling air fraction, at the beginning the far and caf does not significantly change with increasing r_p. After a specific point, the larger r_p will result in the decrease of far and increase of caf. Moreover, far and caf bear a direct and indirect relationship with altitude gain (Figure 11).
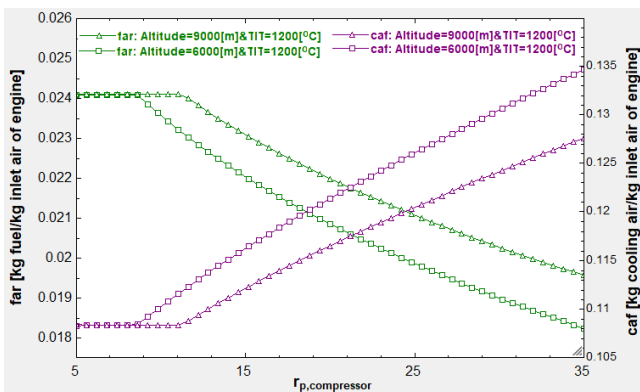

Figure 11. Change curves of caf and far vs. $r_{p,comp}$ at TIT=1200 °C and different altitudes for turboshaft engine.

Figure 12 shows that at 9 km altitude and for optimum exergy efficiency about 4%, 80%, and 16% of entire cycle exergy-destructions occur in the compressor, combustion chamber, and turbine, respectively. The highest amount of Ex_D belongs to the combustion chamber, followed by the turbine and compressor.

Figure 12. Bar plot of exergy destructions (Ex_D) of components at altitude 9000 m, TIT=1200 °C and $\eta_{II,max}$=45.73 for turboshaft engine.

The highest amount of η_{II} belongs to the compressor (97%), followed by the turbine (94%) and combustion chamber (74%) at 9 km altitude as shown in Figure 13.
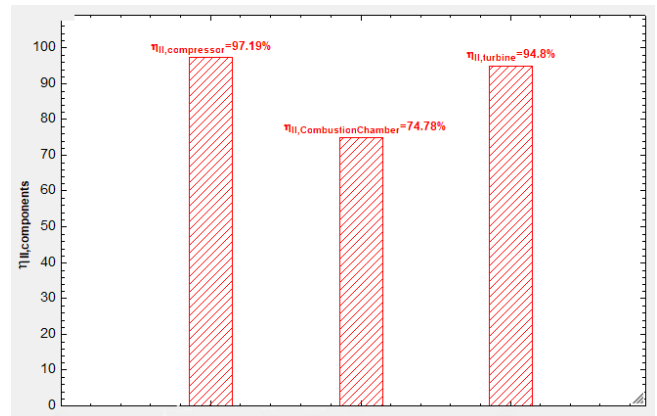
Figure 13. Bar plot of exergy efficiency (η_{II}) of components at altitude 9000 m, TIT=1200 °C and $\eta_{II,max}$=45.73 for turboshaft engine.

5. Conclusion

The thermodynamics optimization and energy-exergy analyses have been done for a turboshaft engine equipped with turbine blades' cooling in different ambient air conditions at different flight altitudes. Results show that:

At the sea level:

- The temperature of ambient air plays an important role in the performance of the turboshaft engine.
- The temperature drop will lead to significant increase in the specific net-work, energy and exergy efficiencies of the cycle.
- In optimum exergy efficiency of entire cycle about 6%, 73%, and 21% of entire cycle exergy-destructions occurs in the compressor, combustion chamber and turbine, respectively. The highest exergy destruction belongs to the combustion chamber, followed by the turbine and compressor.
- The highest exergy efficiency belongs to the compressor (97%), followed by the turbine (94%) and combustion chamber (71%).

At high altitudes:

- The inlet air temperature and density respectively bear indirect and direct relationships with the specific net-work of the turboshaft engine.

- The temperature drop of ambient air plays dominant role and lead to a major increase in the specific net-work of the turboshaft engine with altitude gain from 6 km to 9 km.
- Both energy and exergy efficiencies are slightly increasing with altitude gain.
- At 9 km altitude and for optimum exergy efficiency of entire cycle about 4%, 80%, and 16% of entire cycle exergy-destructions occur in the compressor, combustion chamber, and turbine, respectively. Again, the highest exergy destruction belongs to the combustion chamber, followed by the turbine and compressor.
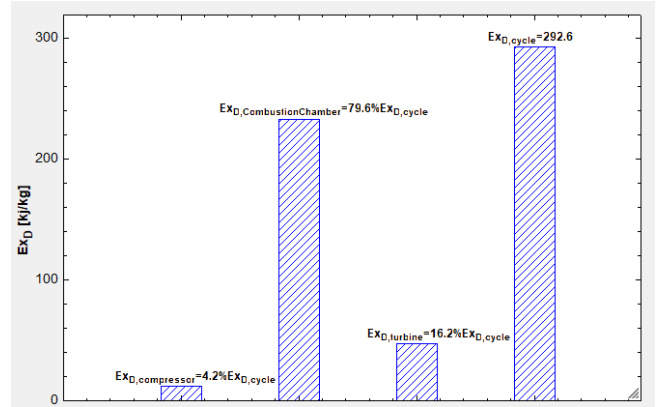- The highest exergy efficiency belongs to the compressor (97%), followed by the turbine (94%) and combustion chamber (74%) at 9 km altitude.

  For all flight scenarios:
- The fuel consumption is larger for lower air temperatures to achieve the same turbine inlet temperature.
- On the contrary, the decrease in air temperature enlarges the cooling capacity, consequently, the cooling air fraction required for turbine blades decreases.

Nomenclature

c_p	specific heat capacity at constant pressure	KJ/ Kg.K
e	specific energy	KJ/ Kg
ex	specific exergy	KJ/ Kg
g	gravitational acceleration constant	m/s^2
$\dot{I}$	irreversibilities	kJ/s
M	Molar Mass	gram/mole
$\dot{m}$	mass flow rate	kg/s
P_0	ambient pressure	Pa
P	pressure	Pa
$\dot{Q}$	Heat flux	kJ/s
r_P	Dimensionless pressure ratio	unitless
s	specific entropy	kJ/kg
t	time	s
T	temperature	K
T_0	ambient temperature	K
V	velocity	m/s
$\dot{W}$	Work flux	kJ/s

Greek Symbols

η	Dimensionless efficiency	unitless
λ	Dimensionless excess air	unitless
ρ	density	Kg

Subscripts

I	1st Law or energetic
II	2nd Law or exergetic
air	ambient air
cc	combustion chamber
ch	chemical
comp	compressor
D	destruction
e	exit
i	input
in	inlet
k	kinetic
p	potential
ph	physical
poly	polytropic
Q	thermal
r	rotator
turb	turbine

Abbreviations

caf	cooling air fraction
CIT	compressor inlet temperature
COT	compressor outlet temperature
far	fuel air ratio
TIT	turbine inlet temperature
TOT	turbine outlet temperature

Appendices
Appendix A. Energy Analysis
Appendix A.1 Mass Conservation (Continuity)

$$\frac{dm}{dt} = \sum \dot{m}_i - \sum \dot{m}_e \tag{A. 1}$$

which $\dot{m}_i$ and $\dot{m}_e$ are the inlet and outlet mass flow rates, respectively.

Appendix A. 2 Energy Conservation (1st Law of Thermodynamics)

$$\frac{dE}{dt} = \dot{Q} - \dot{W} + \sum \dot{m}_i e_i - \sum \dot{m}_e e_e \tag{A. 2}$$

which $\dot{E} = \dot{m}(e)$ and $\dot{Q}$, $\dot{W}$, and e are heat, work, and specific energy, respectively.

$$e = h + \frac{V^2}{2} + gz \tag{A. 3}$$

h, $\frac{V^2}{2}$ and gz are specific enthalpy, kinetic and potential energy terms, respectively.

Appendix A. 3 Entropy Balance (2nd Law of Thermodynamics)

$$\frac{dS}{dt} = \sum_{i=1}^{N} \frac{\dot{Q}_i}{T_i} + \sum \dot{m}_i s_i - \sum \dot{m}_e s_e + \delta \dot{S}_{gen} \tag{A. 4}$$

which $\dot{S} = \dot{m}(s)$, and s is specific entropy.
By restating of this entropy equation, the entropy generation is:

$$\delta \dot{S}_{gen} = \frac{dS}{dt} + \sum \dot{m}_e s_e - \sum \dot{m}_i s_i - \sum_{i=1}^{N} \frac{\dot{Q}_i}{T_i} \tag{A. 5}$$

Based on the Gouy–Stodola theorem, for a control volume with the ambient temperature of T0, the irreversibilities value is calculated as:

$$\dot{I} = T_0 \, \delta \dot{S}_{gen} \tag{A. 6}$$

Appendix A. 4 State Equation
The additional equations like state equation of ideal gas, isentropic and polytropic formulas for compressor and turbine efficiencies may be applied to solve the thermodynamic problems.
For the steady state steady flow (SSSF) thermodynamic processes, all the temporal terms equal zero ($\frac{d}{dt} = 0.0$).

Appendix A. 5 Energy or thermal efficiency (1st law efficiency)

$$\eta_I = \eta_{thermal} = \frac{\dot{E}_{benefited}}{\dot{E}_{cost}} \tag{A. 7}$$

When the energy analysis is done, all unknowns (thermodynamic properties) of the cycle are calculated.

Then, simply the exergy analysis is implemented by using the new exergetic definitions of the components and entire cycle.

Appendix B. Exergy Analysis
Appendix B. 1 The Concept of Exergy

$$\text{Energy=Exergy+Anergy} \tag{B. 1}$$

which exergy and anergy are maximum accessible work and non-accessible work, respectively.

Appendix B. 2 Definition of the Environment from the Exergy Analysis Point of View

From the point of view of exergy analysis, the environment of a system is completely in a thermodynamic equilibrium. There are no gradients in the environment, including pressure, temperature, and chemical potential gradients. In addition, it is not possible to obtain work from the interaction of different components of the environment with each other. Therefore, in exergy analysis, the environment is a reference used to evaluate the performance potential of different systems.

The restricted dead state is a state of the substance in which it is in thermal and mechanical equilibrium with the environment. However, they are not in chemical equilibrium with each other. In the restricted dead state, the substance's temperature and pressure are equal to the ambient temperature and pressure, and the velocity and potential energy of the substance are zero. The dead state is a state of the substance in which it is not only in thermal and mechanical equilibrium but also in chemical equilibrium with the surrounding environment.

Appendix B. 3 Restricted Dead State and Dead State

The restricted dead state is a state of the substance in which it is in thermal and mechanical equilibrium with the environment. However, they are not in chemical equilibrium with each other. In the restricted dead state, the substance's temperature and pressure are equal to the ambient temperature and pressure, and the velocity and potential energy of the substance are zero.

The dead state is a state of the substance in which it is not only in thermal and mechanical equilibrium but also in chemical equilibrium with the surrounding environment.

Appendix B. 4 Exergy Balance
For each component:

$$\frac{\text{dEx}}{\text{dt}}=\dot{Q}\left(1-\frac{T_0}{T}\right)-\dot{W}+\sum \dot{m}_i \, ex_i-\sum \dot{m}_e \, ex_e+\dot{Ex}_D \tag{B. 2}$$

which $\dot{Ex}=\dot{m}(ex)$, and $\dot{Ex}_D$ is the exergy destruction of a component defined as:

$$\dot{Ex}_D=\dot{I}=T_0 \, \delta\dot{S}_{gen}=T_0 \, (\dot{m} \, \delta s_{gen}) \tag{B. 3}$$

which $\dot{I}$ is the irreversibilities value and $\delta\dot{S}_{gen}$ is the entropy generation of a thermodynamic process because of irreversibilities.

For the entire cycle:

$$\frac{\text{dEx}}{\text{dt}}=\dot{Q}\left(1-\frac{T_0}{T}\right)-\dot{W}+\sum \dot{m}_i \, ex_i-\sum \dot{m}_e \, ex_e+ \\ \dot{Ex}_{D,cycle}+\dot{Ex}_{D,loss} \tag{B. 4}$$

which $\dot{Ex}_{D,cycle}$ is the total exergy destruction of a cycle, and $\dot{Ex}_{D,loss}$ is the exergy loss due to the exhaust which is defined as:

$$\dot{Ex}_{D,loss}=\dot{m}_{exhaust} \, \dot{ex}_{exhaust} \tag{B. 5}$$

Again, for the steady state steady flow (SSSF) thermodynamic processes, all the temporal terms equal zero ($\frac{d}{dt}=0.0$).

Appendix B. 5 Exergy Types

In the absence of the effects of nuclear, magnetic, electric, and surface tension fields, the exergy can be written as a summation of physical, chemical, kinetic, potential, and heat transfer exergy parts as:

$$\dot{Ex}=\dot{Ex}_{ph}+\dot{Ex}_{ch}+\dot{Ex}_k+\dot{Ex}_p+\dot{Ex}_Q \tag{B. 6}$$

The physical exergy ($\dot{Ex}_{ph}$) is the maximum accessible work that a substance can do in a reversible process which a substance goes from its initial state to the restricted dead state as:

$$\text{Ex}_{ph}=(h-h_0)-T_0(s-s_0) \tag{B. 7}$$

The chemical exergy ($\dot{Ex}_{ch}$) is the amount of accessible work a substance can do in the chemical equilibrium process surrounded by an environment in which a substance goes from the restricted dead state to the dead state. One of the important applications of the concept of chemical exergy is the calculation of fuel exergy. For hydrocarbon fuels with the form C_nH_m, the amount of chemical exergy is obtained from:

$$\text{Ex}_{ch}=-\Delta g(T_0,P_0)+T_0 R \, \ln\left[\frac{(y_{0,O_2})^{n+\frac{m}{4}}}{(y_{0,CO_2})^n \, (y_{0,H_2O})^m}\right] \tag{B. 8}$$

which R, y, g are the universal gas constant, molar fraction, and Gibbs function, respectively, and:

$$-\Delta g(T_0,P_0)=g(T_0,P_0)_{C_nH_m}-n \, g(T_0,P_0)_{CO_2}-\frac{m}{2} \, g(T_0,P_0)_{H_2O} \tag{B. 9}$$

The chemical exergy of a mixture of ideal gases can be obtained from the following equation:

$$\text{Ex}_{ch}=T_0 \, R \, \sum y_i \, \ln\left(\frac{y_i}{y_{0,i}}\right) \tag{B. 10}$$

The kinetic exergy of equation ($\dot{Ex}_k$) can be calculated as:

$$\text{Ex}_k=m \, \frac{V^2}{2} \tag{B. 11}$$

The potential exergy of equation ($\dot{Ex}_p$) can be obtained as:

$$\text{Ex}_p=m \, g \, z \tag{B. 12}$$

The exergy of heat transfer ($\dot{Ex}_Q$) is the maximum work that can be obtained from the thermal energy transfer as:

$$Ex_Q = Q\left(1-\frac{T_0}{T}\right) \tag{B. 13}$$

Appendix B. 6 Exergy Efficiency (2ⁿᵈ Law Efficiency)

$$\eta_{II} = \frac{\sum \dot{Ex}_{benefited}}{\sum \dot{Ex}_{in}} = 1 - \frac{\sum \dot{Ex}_D}{\sum \dot{Ex}_{in}} \tag{B. 14}$$

Appendix C. Equations

Table C. 1. Equations for Energy-Exergy Analyses.

Components	Related Equations
Compressor	$\dot{m}_2 = (1-caf)\dot{m}_1$ $\dot{W}_{comp} = \dot{m}_1(e_2-e_1)$ $\eta_{I,comp} = \eta_{poly,comp} = \dfrac{\bar{R}T\frac{dP}{P}}{\bar{C}_{p,air}dT}$ $\dot{Ex}_{D,comp} = \dot{W}_{comp} + \dot{m}_1 ex_1 - \dot{m}_2 ex_2$ $\eta_{II,comp} = \dfrac{(\dot{W}_{comp} - \dot{Ex}_{D,comp})}{\dot{W}_{comp}}100$
Cooling Air Fraction	$T_r = 0.8451 TIT + 136.2, \quad T_r$ and TIT are in °C. $caf = \dfrac{2(1+far)(e_3 - e_r)}{(2e_3 - e_2 - e_r)}$
Combustion Chamber	$\dot{m}_3 = \dot{m}_2 + \dot{m}_f$, which $\dot{m}_f = (far)\dot{m}_1$ $\int_{298.15}^{T_f} \bar{C}_{p,C_nH_m}dT + \lambda\left(n+\frac{m}{4}\right)\int_{298.15}^{T_2}\bar{C}_{p,O_2}dT +$ $\lambda\left(n+\frac{m}{4}\right)3.76\int_{298.15}^{T_2}\bar{C}_{p,N_2}dT +$ $\lambda\left(n+\frac{m}{4}\right)4.76\bar{\omega}_1\int_{298.15}^{T_2}\bar{C}_{p,H_2O}dT =$ $n\int_{298.15}^{TIT}\bar{C}_{p,CO_2}dT + (\lambda-1)\left(n+\frac{m}{4}\right)\int_{298.15}^{TIT}\bar{C}_{p,O_2}dT +$ $3.76\lambda\left(n+\frac{m}{4}\right)\int_{298.15}^{TIT}\bar{C}_{p,N_2}dT +$ $\left[\lambda\left(n+\frac{m}{4}\right)(4.76\bar{\omega}_1)+\frac{m}{2}\right]\int_{298.15}^{TIT}\bar{C}_{p,H_2O}dT$ $far = \dfrac{M_{C_nH_m}}{\lambda\left(n+\frac{m}{4}\right)4.76(1+\bar{\omega}_1)M_{air}\eta_{I,cc}}(1-caf)$ $\dot{Ex}_{D,cc} = \dot{m}_2 ex_2 + \dot{m}_f ex_f - \dot{m}_3 ex_3$ $\eta_{II,cc} = \left[1-\dfrac{\dot{Ex}_{D,cc}}{(far)\dot{m}_1 ex_f}\right]100$
Turbine	$\dot{m}_4 = (1+far)\dot{m}_1$ $\dot{W}_{turb} = (caf)\dot{m}_1 e_2 + \dot{m}_3 e_3 - \dot{m}_4 e_4$ $\eta_{I,turb} = \eta_{poly,turb} = \dfrac{\bar{C}_{p,g}dT}{\bar{R}T\frac{dP}{P}}$ $\dot{Ex}_{D,turb} = \dot{m}_3 ex_3 + (caf)\dot{m}_1 ex_2 - \dot{m}_4 ex_4 - \dot{W}_{turb}$ $\eta_{II,turb} = \dfrac{\dot{W}_{turb}}{(\dot{W}_{turb} + \dot{Ex}_{D,turb})}100$
Cycle	$\dot{W}_{net} = (\dot{W}_{turb} - \dot{W}_{comp})\eta_{mech}$ $\eta_{I,cycle} = \dfrac{\dot{W}_{net}}{(far)\dot{m}_1 LHV}100$ $\dot{Ex}_{D,cycle} = \dot{Ex}_{D,comp} + \dot{Ex}_{D,cc} + \dot{Ex}_{D,turb}$ $\eta_{II,cycle} = \dfrac{\dot{W}_{net}}{(far)\dot{m}_1 ex_f}100$

References:

[1] K. Coban, C. O. Colpan, and T. H. Karakoc, "Application of thermodynamic laws on a military helicopter engine," *Energy*, vol. 140, pp. 1427–1436, 2017.

[2] V. Zare, S. Khodaparast, and E. Shayan, "Comparative thermoeconomic analysis of using different jet fuels in a turboshaft engine for aviation applications," *AUT Journal of Mechanical Engineering*, vol. 5, no. 2, pp. 297–312, 2021.

[3] A. Bejan and D. L. Siems, "The need for exergy analysis and thermodynamic optimization in aircraft development," *Exergy, An International Journal*, vol. 1, no. 1, pp. 14–24, 2001.

[4] E. Koruyucu, O. Altuntas, and T. H. Karakoc, "Exergetic investigation of a turboshaft helicopter engine related to engine power," *SAE International Journal of Aerospace*, vol. 13, no. 01-13-02-0019, pp. 257–267, 2020.

[5] O. Balli, "Exergetic, sustainability and environmental assessments of a turboshaft engine used on helicopter," *Energy*, vol. 276, p. 127593, 2023.

[6] G. Tsatsaronis, "Strengths and limitations of exergy analysis," in *Thermodynamic optimization of complex energy systems,* A. Bejan and E. Mamut, Ed., New York, NY, USA, Springer, 1999, pp. 93–100.

[7] I. Dincer and M. A. Rosen, *Exergy: energy, environment and sustainable development,* Oxford, U.K., Elsevier, 2012.

[8] D. Riggins and C. Clinton, "Thrust modeling for hypersonic engines," presented at the International Aerospace Planes and Hypersonics Technologies, Chattanooga, TN, USA, Apr. 3–7, 1995, p. 6081.

[9] D. Riggins, "High-speed engine/component performance assessment using exergy and thrust-based methods," NASA Technical Reports Server, USA, Tech. Rep. NASA CR-198271, 1996.

[10] D. Riggins, "The evaluation of performance losses in multi-dimensional propulsive flows," presented at the 34th Aerospace Sciences Meeting and Exhibit, Missouri, Rolla Univ., USA, Jan. 15–18, 1996, p. 375.

[11] D. Riggins, "Brayton cycle engine/component performance assessment using energy and thrust-based methods," presented at the 32nd Joint Propulsion Conference and Exhibit, Missouri, Rolla Univ., USA, Jul. 15–18, 1996, p. 2922.

[12] D. W. Riggins, "Evaluation of performance loss methods for high-speed engines and engine components," *Journal of Propulsion and Power*, vol. 13, no. 2, pp. 296–304, 1997.

[13] D. Riggins, "The thermodynamic continuum of jet engine performance: the principle of lost work due to irreversibility in aerospace systems," *International Journal of Thermodynamics*, vol. 6, no. 3, pp. 107–120, 2003.

[14] D. W. Riggins, T. Taylor, and D. J. Moorhouse, "Methodology for performance analysis of aerospace vehicles using the laws of thermodynamics," *Journal of Aircraft*, vol. 43, no. 4, pp. 953–963, 2006.

[15] E. T. Curran and R. R. Craig, "The use of stream thrust concepts for the approximate evaluation of hypersonic ramjet engine performance," Wright-Patterson Air Force Aero Propulsion Laboratory, Dayton, OH, USA, Tech. Rep. AFAPL-TR-73-38, 1973.

[16] H. Brilliant, "Analysis of scramjet engines using exergy methods," presented at the 31st Joint Propulsion

Conference and Exhibit, San Diego, CA, USA, Jul. 10–12, 1995, p. 2767.

[17] J. Horlock, "Thermodynamic availability and propulsion," *American Institute of Aeronautics and Astronautics*, vol. 6, pp. 99–741, 1999.

[18] J. Etele and M. A. Rosen, "The impact of reference environment selection on the exergy efficiencies of aerospace engines," presented at the ASME International Mechanical Engineering Congress and Exposition, vol. 16509, Nashville, Tennessee, USA, Nov. 14–19, 1999, pp. 583–591.

[19] M. A. Rosen and J. Etele, "Aerospace systems and exergy analysis: applications and methodology development needs," *International Journal of Exergy*, vol. 1, no. 4, pp. 411–425, 2004.

[20] D. L. Hunt, R. M. Cummings, and M. B. Giles, "Wake integration for three-dimensional flowfield computations: Applications," *Journal of aircraft*, vol. 36, no. 2, pp. 366–373, 1999.

[21] M. B. Giles and R. M. Cummings, "Wake integration for three-dimensional flowfield computations: theoretical development," *Journal of aircraft*, vol. 36, no. 2, pp. 357–365, 1999.

[22] D. Moorhouse, H. Charles, and J. Prendergast, "Thermal analysis of hypersonic inlet flow with exergy-based design methods," *International Journal of Thermodynamics*, vol. 5, no. 4, pp. 161–168, 2002.

[23] K. A. B. Pathirathna, "Gas turbine thermodynamic and performance analysis methods using available catalog data," M.Sc. thesis, Dept. Engineering and Sustainable Development, Univ. Gävle, Gävle, Sweden, 2013. [Online].Available:https://avys.omu.edu.tr/storage/app/public/ozcanh/111428/MMB718-3.pdf

[24] V. Amati, C. Bruno, D. Simone, and E. Sciubba, "Exergy analysis of hypersonic propulsion systems: Performance comparison of two different scramjet configurations at cruise conditions," *Energy*, vol. 33, no. 2, pp. 116–129, 2008.

[25] D. F. Rancruel and M. R. von Spakovsky, "Decomposition with thermoeconomic isolation applied to the optimal synthesis/design and operation of an advanced tactical aircraft system," *Energy*, vol. 31, no. 15, pp. 3327–3341, 2006.

[26] E. T. Turgut, T. H. Karakoc, and A. Hepbasli, "Exergoeconomic analysis of an aircraft turbofan engine," *International Journal of Exergy*, vol. 6, no. 3, pp. 277–294, 2009.

[27] M. Fallah, A. Sohrabi, and N. H. Mokarram, "Proposal and energy, exergy, economic, and environmental analyses of a novel combined cooling and power (ccp) system," *Journal of the Brazilian Society of Mechanical Sciences and Engineering*, vol. 45, no. 9, p. 441, 2023.

[28] G. C. Oates, *Aerothermodynamics of gas turbine and rocket propulsion,* Reston, VA, USA, AIAA, 1997.

[29] J. D. Mattingly, K. M. Boyer, and H. von Ohain, *Elements of propulsion: gas turbines and rockets*, Reston, VA, USA, AIAA, 2006.

[30] R. Langton and B. MacIsaac, *Gas turbine propulsion systems*, Hoboken, NJ, USA, John Wiley & Sons, 2011.

[31] A. F. El-Sayed, *Fundamentals of aircraft and rocket propulsion*, London, U.K., Springer, 2016.

[32] A. F. El-Sayed, *Aircraft propulsion and gas turbine engines*, Boca Raton, FL, USA, CRC press, 2017.

[33] J. Van Wylen and E. Sonntag, *Fundamental of Classical Thermodynamics*, Hoboken, NJ, USA, John Wiley & Sons, 1998.

[34] K. Annamalai, I. K. Puri, and M. A. Jog, *Advanced thermodynamics engineering*, Boca Raton, FL, USA, CRC press, 2010.

[35] D. Winterbone and A. Turan, *Advanced thermodynamics for engineers*, Oxford, U.K., Butterworth-Heinemann, 2015.

[36] A. Bejan, *Advanced engineering thermodynamics,* Hoboken, NJ, USA, John Wiley & Sons, 2016.

[37] M. Tabatabaian, *Advanced Thermodynamics*, Herndon, VA, USA, Mercury Learning & Information, 2017.

[38] C. Borgnakke and R. E. Sonntag, *Fundamentals of thermodynamics,* Hoboken, NJ, USA, John Wiley & Sons, 2022.

[39] M. Yari and K. Sarabchi, "Comparative investigation of various humidified gas turbine cycles," presented at the Turbo Expo: Power for Land, Sea, and Air, ASME, vol. 41723, Vienna, Austria, Jun. 14–17, 2004, pp. 693–703.

[40] K. Sarabchi, "Performance evaluation of reheat gas turbine cycles," *Proceedings of the Institution of Mechanical Engineers*, Part A: Journal of Power and Energy, vol. 218, no. 7, pp. 529–539, 2004.

[41] M. Fallah, H. Siyahi, R. A. Ghiasi, S. Mahmoudi, M. Yari, and M. Rosen, "Comparison of different gas turbine cycles and advanced exergy analysis of the most effective," *Energy*, vol. 116, pp. 701–715, 2016.

[42] P. Charbonneau, "An introduction to genetic algorithms for numerical optimization," *NCAR Technical Note,* vol. 74, pp. 4–13, 2002.

Research Article

Experimental and Numerical Investigation of Roughness Structure in Wind Turbine Airfoil at Low Reynolds Number

[1*]H. E. Tanürün (ID), [2]A. G. Akın (ID), [3]A. Acır (ID), [4]İ. Şahin (ID)

[1]Kahramanmaraş Istiklal University, Elbistan Engineering Faculty, Department of Energy Systems Engineering, Kahramanmaraş, Türkiye
[2]T.C. Presidency of Defense Industries, Naval Platforms Department, Ankara, Turkey
[3]Gazi University, Faculty of Technology, Department of Energy Systems Engineering, Ankara, Turkey
[4] Purdue University, School of Mechanical Engineering, West Lafayette, 47906, USA
E-mail: [1*]erdi.tanurun@istiklal.edu.tr

Abstract

This paper experimentally and numerically investigates the effects of suction side surface roughness on the aerodynamic performances of the NACA 0015 turbine blade profile. Three different NACA 0015 turbine blade configurations, which are smooth (K_0), single roughness (K_1), and double roughness (K_2), are considered. The experimental studies were conducted using the HM-170 GUNT open wind tunnel model. The aerodynamic characteristics of these three blade configurations are evaluated in terms of their lift coefficient (C_L), drag coefficient (C_D), and aerodynamic efficiency (C_L/C_D). The maximum C_L ($C_{L,max}$) for K_0 was obtained at 25°, whereas the $C_{L,max}$ angles for the K_1 and K_2 roughness blade profiles were reduced to 22.5°, utilizing the rough surfaces on the suction side. The experimental analysis revealed that the K_2 profile demonstrated a 21% and 19% enhancement in maximal C_L over the K_0 and K_1 profiles, respectively. The highest C_L/C_D was observed with K_1, except at low attack of angle (αoα), where the smooth blade profile resulted in slightly better performance. Experimental analysis showed peak C_L/C_D at αoα of 7.5° for K_0, and 12.5° for both K_1 and K_2, with K_1's optimal C_L/C_D being 2.85% and 8.5% higher than K_0 and K_2, respectively. Numerical analysis indicated that the $C_L/C_{D,avg}$ for K_1 was observed to be 11% and 8% higher than that of K_0 across all αoα.
.

Keywords: Airfoil; roughness; aerodynamic performance; passive flow control; experimental.

1. Introduction

The increase in living standards leads to a rise in energy demand. Due to the finite nature of fossil resources and their harmful emissions to the environment, finding alternatives to these resources and more efficient methods of energy production is essential [1-2]. Wind energy is one of these alternative sources. Significant attention has been garnered by wind power within the electricity generation industry due to its easy accessibility and environmental friendly impacts. Hence, enhancements are necessitated for the designs of wind turbines and their components for cost-effective energy conversion. Among these components, a pivotal role in electricity generation is played by the aerodynamic performance of turbine blades, which convert wind energy into mechanical energy. Consequently, the effects of blade design on the aerodynamic performance of wind turbine have been concentrated on by researchers. Researchers have observed stall angles and aerodynamic performances of various symmetrical turbine blade models using both experimental and numerical methods [3-8]. Additionally, the performance of asymmetric blade models, which have become increasingly popular in recent years due to their high efficiency, is also being examined in the literature [9-11].

By employing numerical methods with the k-ε turbulence model, Karthick and Kumar [12] studied the performance coefficients of the NACA 0015 blade profile at αoα ranging from 0 to 20°. Their results were found to concur with those from previous studies on vertical axis wind turbine blades. Rubel et al. [13] experimentally examined the NACA 0015 blade across αoα from 0° to 180°, corroborating their numerical study with experimental outcomes to elucidate how variations in αoα affect the blade's lift coefficients (C_L) and drag coefficients (C_D), and to detail the turbulence, pressure, and velocity distribution around the blade from simulation data. To augment the aerodynamic performance of the NACA 0015 blade profile, the suction side of the trailing edge region was modified with backward steps by Kabir et al. [14], reporting a decrease in C_D attributable to these modifications.

The influence of aspect ratio (AR) on blade aerodynamic performance and stall angle behavior has been documented [15]. The aerodynamic performance of turbine blades at low Reynolds numbers (RE) by altering ARs was experimentally probed by Mizoguchi et al. [16], highlighting that the flow structure at low ARs diverges from that at high ARs at substantial αoα.

To regulate airflow over platforms using blade structures, especially in wind turbines, various flow control methods have been devised. These controls are categorized into active and passive flow control methods. It is marked by the

principal distinction between these flow control strategies that, unlike passive control, which does not require external energy, active control necessitates it. Techniques such as dimples, tubercles [17], vortex generators (including various types of flaps [18-19], wind lenses [20-21], and rough surfaces are widely adopted in the implementation of passive control methods.

In the operational context of wind turbines, the blades are subjected to adverse conditions such as dust, sand, ice, and material deformation, leading to surface roughness. A comprehensive understanding of how surface roughness influences the aerodynamic performance of turbine blades has been necessitated, a topic that has garnered increased focus in recent research efforts. Inspired by the rough regions on the wing surfaces of organisms such as bald eagles and dragonflies, rough areas have been integrated onto the airfoil surface. These applications have begun to be implemented experimentally and are anticipated to be commercialized in the near future [22]. An experimental examination of the aerodynamic consequences of surface roughness on the NACA 0012 profile was undertaken by Chakroun et al. [23], observing a beneficial impact of trailing edge roughness on both the C_L and C_D. In a similar vein, into the effects of micro-scale roughness on blade aerodynamics was delved by Salazar and Barrientos [24], employing angular speckle correlation for roughness assessment and introducing a mathematical formula to quantify uncertainty. The aerodynamic losses attributable to surface roughness were focused on by Zhang et al. [25] through their experimental work, whereas the aerodynamic ramifications of deformations at the leading and trailing edges of blades were explored by Wang et al. [26], proposing a modified NACA 0012 blade profile optimized for vertical axis wind turbines.

Further contributing to this body of work, a numerical analysis on the roughness effects pertinent to blades used in micro air vehicles was conducted by El-Latief et al. [27], comparing the aerodynamic performance of smooth versus roughness blade profiles at ultra-low Reynolds numbers (Re = 1400) and demonstrating a superior C_L for the roughness configuration. Echoing these findings, the superior aerodynamic performance of roughness blade profiles compared to smooth ones at low RE for micro air vehicles was confirmed by Murphy and Hu [28], attributing the enhanced lift to changes in vortex formation and turbulent flow patterns induced by roughness surfaces. The impact of roughness surfaces on turbine blade performance was investigated by Tamai et al. [29], noting that such profiles facilitate an expedited transition from laminar to turbulent flow at low RE, thereby boosting aerodynamic efficiency. Experimental investigations to ascertain how wake turbulence influences blade performance under transonic flow conditions were conducted by Zhang and Ligrani [30]. It was demonstrated that the enhanced flow diffusion region at the suction side of the trailing edge causes wake formation to be significantly influenced by the surface roughness factor. Similarly, the C_L and C_D performances of both smooth and roughness NACA 0012 turbine profiles, utilizing a combination of experimental and numerical methodologies, were assessed by Xia et al. [31]. By varying the angle of attack ($\alpha o \alpha$), the behaviors of C_L and C_D were documented, noting an improvement in the C_L/C_D for roughness blade profiles at lower $\alpha o \alpha$ compared to smooth profiles.

Liu et al. study on a NACA 23012 revealed that initial ice roughness significantly impacts water film and flow, notably retarding primary wave formation at U_∞=10 m/s and causing

rivulets to merge at higher speeds (15 m/s), thus affecting surface water/ice dynamics [32]. Sun et al. proposed a novel multi-objective evolution algorithm to enhance the aerodynamic performance of the NACA2415, mitigating cavitation and surface roughness effects, which resulted in a 20% average increase in the C_L/C_D and a 17.2% average reduction in the minimum peak lift coefficient [33]. Wang et al. study demonstrates that surface roughness, with a magnitude of Ra=157µm, covering 10%, 30%, 50%, and 100% of the suction surface, leads to a respective decrease in profile loss of 14.6%, 16.04%, 16.45%, and 10.20%, highlighting the effective role of surface roughness on aerodynamic performance [34]. Özkan and Erkan's study on the NACA 63-415 airfoil showed that while roughness minimally affected aerodynamics at Re≤104, it significantly enhanced performance between Re of $5 \times 10_4$ to $1.5 \times 10_5$, with benefits persisting up to a roughness height of 0.1 mm for Re=$2.5 \times 10_5$, beyond which roughness reduced the C_L/C_D [35]. Kelly et al. study quantitatively demonstrates that blade roughness on wind turbines decreases performance by 2.9–8.6% and that re-optimizing the controller gain coefficient can enhance annual energy production by 0.1–1.0%, highlighting the potential of control strategies to mitigate roughness effects [36]. Dwivedi et al. experimental study on a NACA 4412 at a RE of 1.7×10^5 demonstrates how surface roughness, induced at different chord length (c) areas, significantly affects aerodynamic C_L, C_D and stall characteristics, suggesting the potential for controlled roughness application during takeoff and landing to optimize performance [37].

As indicated by the aforementioned studies, surface roughness plays a crucial role and directly impacts the aerodynamic performance of blades. Initial research efforts were predominantly focused on the effects of roughness on the turbine blades of aircraft, such as helicopters and unmanned aerial vehicles. More recently, the emphasis has shifted towards investigating the impact of roughness on wind turbine blades, particularly in the trailing edge region. Nonetheless, the specific effects of roughness situated near the mid-chord region of the blade and its consequent impact on blade performance warrant further exploration. Hence, this study modifies the suction side of the NACA 0015 with single and double roughness regions, respectively, while employing the smooth NACA 0015 profile as a baseline for comparison. Experiments and numerical simulations were conducted at an inlet flow velocity of 10 m/s, corresponding to a RE of 42,800. Results pertaining to C_L, C_D, and the C_L/C_D were compiled. Data derived from numerical analyses were corroborated with experimental findings, which were further substantiated by pressure, velocity, and turbulence intensity contours from the numerical simulations.

2. Experimental Setup and Procedure
2.1 Wind Tunnel Facility

This study's experimental component utilized the HM-170 GUNT model, an open-type wind turbine depicted in Fig. 1. The wind tunnel is segmented into nozzle, test, and diffuser sections. Air is directed through a honeycomb structure in the nozzle section to ensure a uniform flow velocity with minimal turbulence before it accelerates towards the test section. Measurements were conducted exclusively within the test section, characterized by a square cross-section measuring 0.3x0.3 m^2 and extending 0.4 m in length, allowing air to maintain a steady and laminar velocity until it reaches the diffuser section.

At the test section's inlet, pressure parameters and the free-stream velocity (V_∞) are measured using a pitot tube and an inclined manometer, respectively. Based on a wind speed of 10 m/s, experimental and numerical tests were performed by varying the αoα from 0 to 35°, with a Re of 42,800 as the basis. The blade model is centrally mounted in the test section on a metal rod, one end of which connects to a force sensor situated beneath the test section, and the other end affixes to the blade. This setup enables the force sensor to detect two principal force components acting on the blade model: the drag force aligned with the airflow and the lift force acting perpendicular to it.

Given the test section's limited cross-sectional area, a blockage ratio is employed to mitigate the sidewall effects on the blade's flow characteristics. This ratio, which is the blade's surface area relative to the test section's cross-sectional area, is recommended not to exceed 10% [38]. For this study, the blockage ratio was calculated to be 8.9%, obviating the need for any blockage-related corrections.
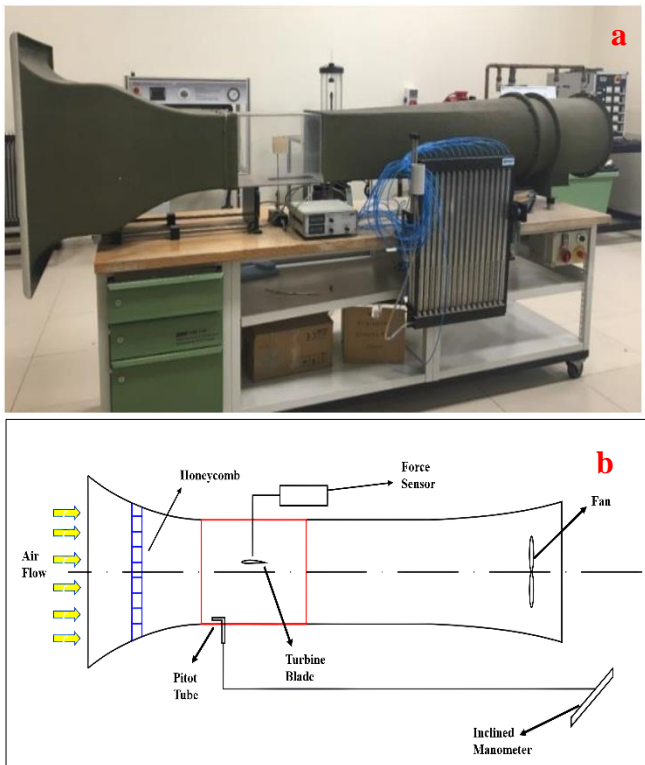

Figure 1. Schematic and Experimental views of Wind tunnel.

2.2 Blade Configurations

To elucidate the impact of roughness surfaces on aerodynamic performance, symmetrical blade models, which are commonly employed in wind turbines and unmanned aircraft, are utilized. This approach enables the identification of how roughness surfaces influence flow separation and reattachment, particularly at a 0°, by comparing the effects on pressure (smooth) and suction (roughness) sides. For this purpose, the study employs a symmetrical NACA (National Advisory Committee for Aeronautics) 0015 four-digit model for experimental investigations. The blade's coordinate data was sourced from the "NACA 4 digit blade generator" [39] as shown in Fig. 2.a Design software was employed to produce three versions of the blade model: a smooth blade model (K_0), a single roughness blade model (K_1), and a double roughness blade model (K_2). Details of the schematic and experimental models are presented in Fig. 3 and Fig. 4, respectively. For all airfoil, the c has been set at 66 mm.
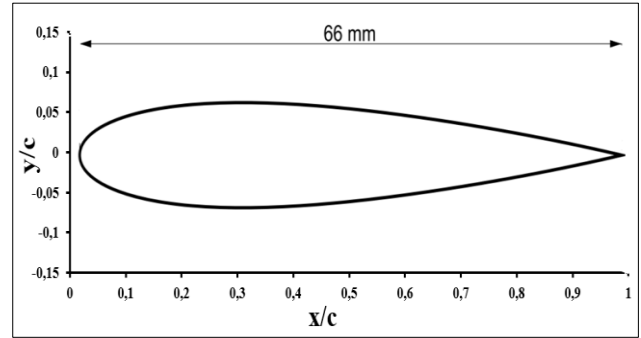

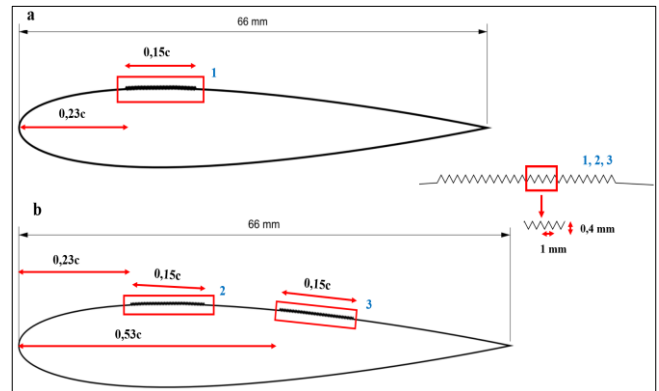Figure 2. Schematic structure of NACA-0015 turbine blade profile (Smooth blade, K_o).

Figure 3. Geometric description of a) K_1 and b) K_2.

In this study, the variation of turbulence and laminar boundary layers in response to an increasing αoα on the blade surface is systematically explored, with an emphasis on the differential impacts of rough versus smooth surface treatments on aerodynamic performance. As depicted in Fig. 3a, a unique roughness configuration (K_1) is engineered on the suction side of the blade, incorporating a spanwise-width roughened area extending 0.15c in length from 0.23c to the leading edge. Given that the onset of turbulent flow begins at the trailing edge, an additional roughness structure is integrated to enhance performance at lower αoαs, resulting in the development of the K_2 profile, as illustrated in Fig. 3b. The initial rough surface is situated 0.23c from the leading edge, while the subsequent one is located 0.53c from the leading edge, with each roughness width uniformly maintained at 0.15c. A primary objective of this study is to delay flow separation on the blade surface by employing surface roughness, aiming to enhance the aerodynamic performance. This model specifically seeks to quantify the influence of surface roughness on blade efficacy within the turbulent boundary layer zone on the suction side.
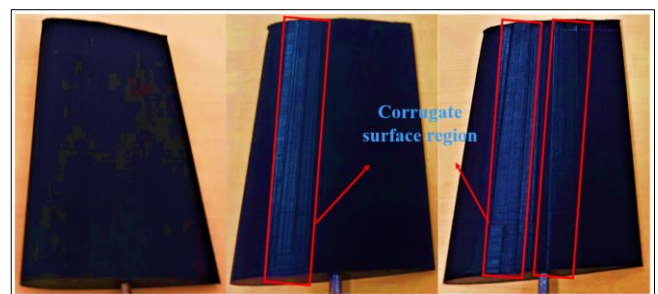

Figure 4. a) Smooth surface b) single and, c) double roughness blade models produced by 3D printer.

The blades utilized in the experimental phase were fabricated using an Ultimaker extended 3D printer. Aerodynamic studies frequently employ a diverse array of materials in the construction of blade models. A primary objective of this study is to minimize surface roughness to accurately capture the blade profile. Consequently, due to its minimal material roughness effect, CPA+ type filament was selected for the production of the blade profile.

To verify the blades' surface roughness quality after the manufacturing process, measurements were conducted using a Mitutoyo J-412 (shown in Fig. 5) 90° / 5 μm Surface Roughness Magnitude (R_a) Tester. The roughness values were assessed at two distinct areas: the blade's smooth surface and the roughness structure. Measurements were taken three times from both the smooth and roughness surfaces of the K_2 model, and their average values were considered for the numerical analysis. According to the sensor's findings, the roughness of the smooth and roughness surfaces was measured to be 1.062 μm and 6.267 μm, respectively.

Table 1. Roughness of the plain and roughness surfaces of the blades model.

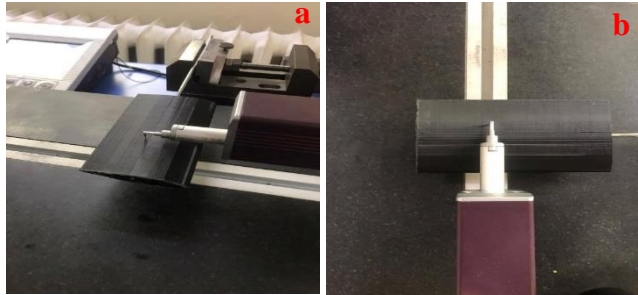| Measurement	1.	2.	3.	Measurement$_{AVG}$
Smooth Surface(μm)	1,061	0,903	1,224	1,062
Roughness Surface(μm)	6,122	6,014	6,665	6,267

Figure 5. a) Isometric and b) top view of the blades surface during roughness measurements.

There are two non-dimensional coefficients existing for describing the effect of lift and drag forces on the turbine blade profile. Lift coefficient (C_L) and drag coefficient (C_D) are being used to detect the aerodynamic performance of blade [40].

Lift Coefficient:

$$C_L = \frac{2L}{\rho V^2 A} \quad (1)$$

Drag Coefficient:

$$C_D = \frac{2D}{\rho V^2 A} \quad (2)$$

Eq. 3 defines the average aerodynamic performance, which helps in understanding the positive effects of surface roughness on blade performance.

$$C_L/C_{D\,avg} = \frac{\Sigma^{C_L}/_{C_D}}{k} \quad (3)$$

k is the total number of αoα.

2.3 Experimental Uncertainty

Experimental results inherently contain uncertainties, which can be minimized but not completely eliminated. The primary sources of these uncertainties include errors from devices, tools, and materials used during the experiments. The most important factor affecting accuracy is errors that may arise from different reasons during experiments such as error factor of the devices, tools, and materials utilized during the tests. Uncertainties of the devices documented in Table 2, and by using equations 4 and 5 uncertainties for C_L and C_D are calculated and given in Table 3. As seen in Table 3, the obtained uncertainties C_L and C_D are respectively ± 0,036 and ± 0,031. Kline and McClintock methods were used in the uncertainty analysis of the measurement devices used in the experimental study [41]. By using this method, the effect of each variable on the total uncertainty has been taken into account in the expressions in Eq. 5 and 6.

$$R = R(X_1, X_2, X_3, \quad X_N,) \quad (4)$$

$$W_R = \sqrt{\left(\frac{\partial R}{\partial x_1}w_1\right)^2 + \left(\frac{\partial R}{\partial x_2}w_2\right)^2 + \left(\frac{\partial R}{\partial x_3}w_3\right)^2 + \cdots + \left(\frac{\partial R}{\partial x_N}w_N\right)^2} \quad (5)$$

Table 2. Uncertainties for Measuring Instruments.

Measuring device	Uncertainty
Length Measurement (Caliper)	± 2x10^{-5} m
Velocity Measurement (Anemometer)	± 0,10 m/s
Pressure Measurement (Pitot tube)	±0,015 Pa
Force Measurement (Load cell)	± 0,014 N
Roughness surface Measurement (roughness tester)	±0,01 (μm)

Table 3. Maximum uncertainties for calculations.

Calculate	Uncertainty
Lift Coefficient (C_L)	± 0,036
Drag Coefficient (C_D)	± 0,031

3. Numerical Study Setup
3.1 Computational Domain and Mesh

In order to detailedly investigate the flow behavior around the blade models, in the current work, the experiments are supported by numerical simulation. A C-type flow domain is considered to have a cost-effective numerical solution. To reduce the effects of the side boundaries on the blade models, the C-type flow domain is decided to be 36c by 45c, shown in Fig. 6.
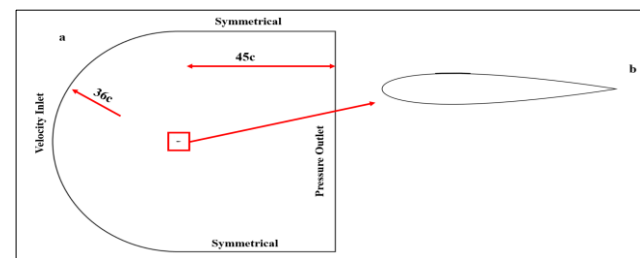

Figure 6. a) C-type domain b) K_1 model.

The curved side of the C-type flow was set with velocity inlet boundary conditions. Therefore, by changing the inlet flow direction, the αoα is adjusted. The inlet flow velocity magnitude is set based on the experimental conditions.

Pressure outlet is used as an exit boundary condition. The numerical solution was performed using Ansys-Fluent.

The mesh was created in the Ansys-Meshing tool by using triangular and rectangular elements. Due to the large velocity and pressure variations in the velocity boundary layer areas on the blade surface, a densified mesh was applied with the edge size command in order to obtain a quality solution. Mesh structure is involved on the Fig. 7a and 7b.
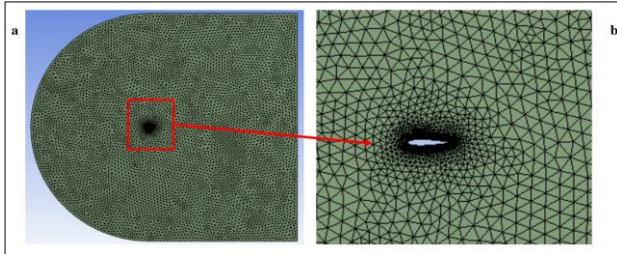

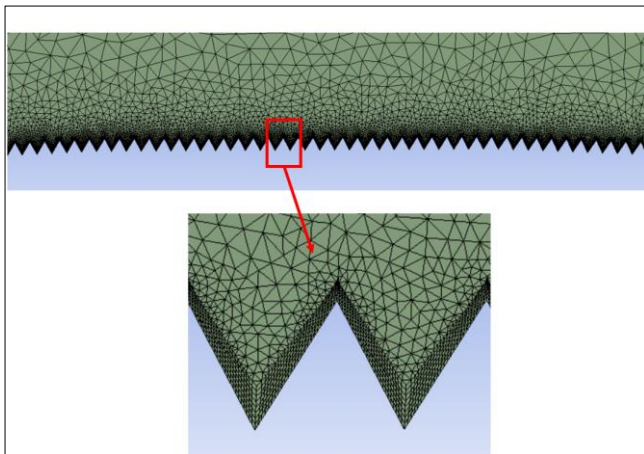*Figure 7. Numerical model mesh: (a) view of the entire domain and (b) close view of the domain.*

Figure 8. Mesh structure around roughness surface.

To ensure the quality of the numerical solution, mesh independency was applied for K_0 profile. The number elements were increased from 100 946 to 194 978 as seen in Table 4, and solution was obtained at 17.5° αoα. The difference between results around 0.1% is assumed to be good enough; therefore, mesh including 128 986 elements was chosen for smooth blade solution.

Table 4. Independence of Elements amount.

	C_L	C_D	Mesh Elements
	0.9234	0.2848	100946
Smooth Surface (K_0)	**0.9311**	**0.2859**	**128986**
	0.9320	0.2887	145626
	0.9319	0.2872	153484
	0.9417	0.2871	194978

In addition to mesh independence; mesh quality of the smooth blade is documented based on well-known parameters which are element quality, orthogonal quality and skewness [42]. It is recommended that the values of element quality and orthogonal quality close to 1, while the skewness is close to 0. Also, by considering these qualities of smooth and roughness blades meshes were created and their information is given in Table 5. In addition, Fig. 8 is provided to show details of a mesh around roughness region.

Table 5. Mesh Specifications.

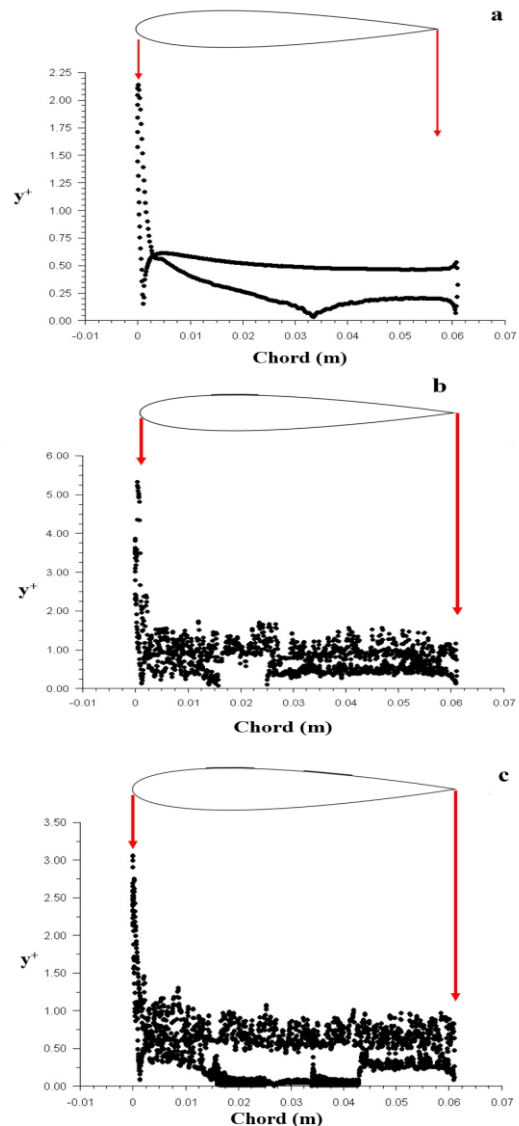| Mesh Quality	Elements	Element Quality	Orthogonal Quality	Skewness
(K_0)	128986	0.9332	0.9332	0.0433
(K_1)	219000	0.9710	0.9710	0.0432
(K_2)	260000	0.9704	0.9704	0.0434

Figure 9. y^+ at 22.5° a) K_0, b)K_1 and c)K_2.

Mesh structure and configuration around the blade are very crucial to achieve a more precise result. y^+ is a nondimensional coefficient and describes thickness of boundary layers [42].

$$y^+ = \frac{U_*.y}{\upsilon} \tag{6}$$

Eq. 6 [43] shows dimensionless y^+ equation, where U* is the friction velocity, y is the distance of the wall and υ is the local kinematic viscosity of the fluid. Boundary layers are divided into 4 regions which are called viscous sub-layer ($y^+ \leq 5$), buffer layer ($5 < y^+ \leq 30$), log-law region ($30 < y^+ \leq 500$) and outer layer [44-45]. In addition to mesh sizes and qualities, to show the credibility of the numerical solutions obtained in the current study, y^+ values where plotted in Fig. 9 for each blade configuration at 17.5° αoα. As seen from the figure, except for the leading edges, y^+ values around or lower than 2 for each configuration; that is boundary layer development on the blade could be captured during the numerical solutions.

In this paper, the numerical simulations are based on incompressible two dimensional steady-state conditions. For the

sake of completeness, the following mass and momentum conservation equations are provided.

$$\frac{\partial \rho}{\partial t} + \rho \, divV = 0 \tag{7}$$

Specific weight of fluid does not change in time [46]

$$\frac{\partial \rho}{\partial t} = 0 \tag{8}$$

Due to specific weight does not change, continuity equation changes into $divV = 0$ or $\nabla.V = 0$ similarly [46].

Conversation of momentum based on the Newton's second law of motion, expresses a proportionality between applied force and the resulting acceleration of a fluid particle.

$$\rho \frac{DV}{Dt} = \rho g + \nabla.\tau_{ij} \tag{9}$$

3.2 Validation of Turbulence Model

In the realm of numerical analyses, the selection of turbulence models is contingent upon the specific domains of application. To ascertain the turbulence model that exhibits the highest fidelity, the C_L versus αoα trends of four distinct turbulence models—Spalart-Allmaras, k-ε realizable, transition SST, and k-ω SST—were juxtaposed with empirical data. Subsequently, the model that demonstrated the closest alignment with the experimental outcomes was identified.
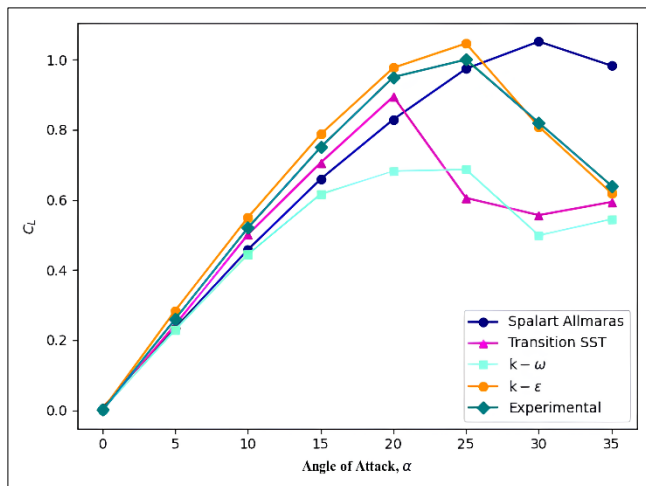

Figure 10. Comparison of C_L values of 4 different turbulence models and experimental study for K_0.

In Fig. 10, the aerodynamic performance of the K_0, as delineated by the C_L versus αoα graph, is juxtaposed against the outcomes derived from various turbulence models. Within the 0 to 5° αoα range, the discrepancies between the C_L values obtained from the experimental investigation and those predicted by the four turbulence models are negligible. However, post-5°, variations in solution accuracy—attributable to turbulence manifesting on the blade surfaces—culminate in discernible deviations among the results yielded by different turbulence models on the graph. Consequently, while the experimental data exhibit variances in comparison to the outcomes of the Spalart-Allmaras and k-ω turbulence models, the Transition SST and k-ε realizable models demonstrate parallel accelerations. With an escalation in αoα, and the ensuing turbulence engendered by vortices over a substantial portion of the blade surface, it was noted that all turbulence models, with the exception of the k-

ε realizable model, diverged markedly from the experimental findings. Owing to its congruency in stall angle values and its close alignment with experimental data at elevated αoα, the k-ε realizable model was adjudged the most apt turbulence model for this investigation.

Due to the high compatible with the experimental study, k-ε realizable turbulence model whose equations given in Eq. 10 and Eq. 11 was used to obtain numerical results. Also, k-ε realizable turbulence model has been widely used by researchers [47-48].

For turbulence kinetic energy (k);

$$\frac{\partial}{\partial t}(\rho k) + \frac{\partial}{\partial x_j}(\rho k u_i) = \frac{\partial}{\partial x_j}\left[\left(\mu + \frac{\mu_t}{\sigma_k}\right)\frac{\partial k}{\partial x_j}\right] + G_k + G_b - \rho \epsilon - Y_M + S_k \tag{10}$$

For energy dissipation rate (ε);

$$\frac{\partial}{\partial t}(\rho \epsilon) + \frac{\partial}{\partial x_j}(\rho \epsilon u_i) = \frac{\partial}{\partial x_j}\left[\left(\mu + \frac{\mu_t}{\sigma_\epsilon}\right)\frac{\partial \epsilon}{\partial x_j}\right] + C_1 \frac{\epsilon}{k}(G_k + C_3 G_b) - C_2 \rho \frac{\epsilon^2}{k} + S_\epsilon \tag{11}$$

G_k is described as turbulence kinetic energy due to the velocity and G_b is described as turbulence kinetic energy due to the buoyancy. C is a constant. $\sigma_k \, and \, \sigma_\epsilon$ are turbulent Prandtl numbers.

4. Result and Discussions

In this study, to analyze the NACA 0015 and roughness turbine blade profiles aerodynamic performance such as C_L, C_D, C_L / C_D and turbulence kinetic energy, numerical analysis were conducted by using Ansys Fluent Software for between 0-35° each 2.5° degree. This methodical approach allowed for a comprehensive understanding of the aerodynamic behaviors across a broad range of angles, enhancing the reliability of the results.
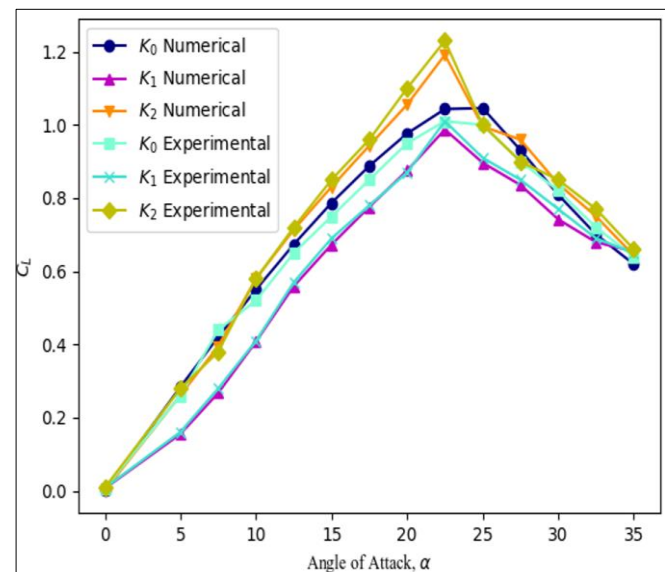

Figure 11. Comparison of C_L values of K_0, K_1 and K_2.

In Fig. 11, the C_L values for the K_0, K_1, and K_2 across the 0-35° αoα range were subjected to both numerical and experimental analysis. Up to a 20° αoα, the behavior of K_0 and K_2 was observed to be analogous. This similarity indicates consistent performance characteristics between

these two models under lower angle conditions. At these αoα, the K_1 blade model exhibited lower C_L values in comparison to its counterparts. The stall angles for the K_1 and K_2 models were identified at 22.5°, whereas the K_0 demonstrated a stall angle at 25. Upon experimental analysis of these metrics, it becomes evident that the maximum C_L performance of the K_2 surpasses that of the K_0 by 19% and the K_1 by 21%. These findings underscore the superior aerodynamic performance of the K_2 model, particularly in post-stall conditions. Both preceding and succeeding the stall point, the K_2 consistently manifested the highest C_L values. At a 35° αoα, the C_L values of the three blade models converge closely. The incorporation of dual roughness structures on the K_2 beyond a 10° αoα, coupled with the emergence of high turbulence density between these structures—as will be elucidated in Fig. 16c—accounts for the superior C_L performance relative to the smooth model. Conversely, the proximal positioning of the roughness structure to the leading edge on the K_1 negates any potential benefits, given that the flow in this region remains laminar at low αoα. Instead, the fluid interaction is confined to the apex of the roughness structure on the blade surface, reducing the contact area and consequently diminishing the drag force in comparison to the other models. Moreover, the restricted flow interaction with the blade's upper surface results in accelerated flow over the smooth blade's upper contour, leading to a reduced pressure differential and thus a lower C_L than that observed in the other two models.

The reason for the lower stall angle is that while rough surfaces increase flow attachment, they also enhance turbulence that can cause earlier flow separation. This is especially true at high αoα, leading to earlier separation of the flow from the airfoil's upper surface and thus, the occurrence of stall at lower angles. This phenomenon underscores the dynamic and complex nature of the impact of rough surfaces on aerodynamic performance.
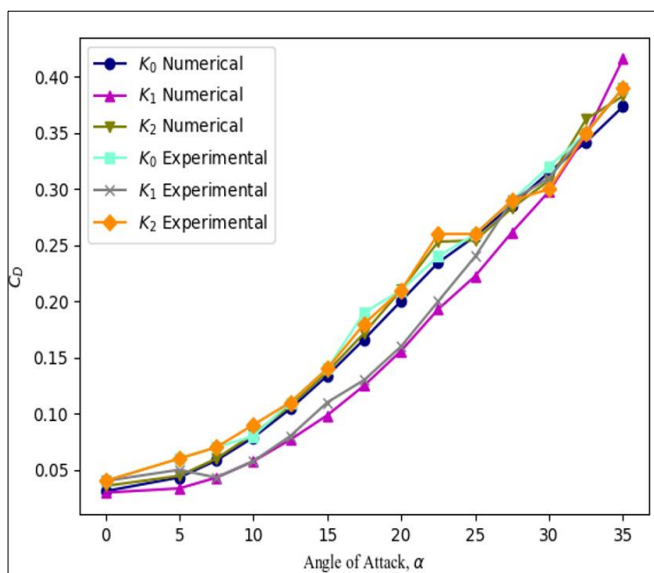

Figure 12. Comparison of C_D values of K_0, K_1 and K_2.

In Fig. 12, the C_D values for the K_0, K_1, and K_2 across the 0-35° αoα range were scrutinized. A negligible variance in C_D was observed among the three blade models within the 0-5° range. In the experimental analysis, it was notably observed that the C_D values for the K_1 were lower than those for the other models from 10-25°. The K_0 and K_2 exhibited analogous behaviors up to a 15° αoα; beyond this point, the

K_2 model demonstrated a steeper ascent in C_D up to 22.5° compared to the K_1. It has been determined that at the stall angle of 22.5°, the C_D of K_2 is 10.41% and 38.46% higher compared to K_1 and K_0, respectively.

In the span between 7.5° and 25°, the K_1 manifested the lowest C_D values relative to the other profiles. Notably, a dramatic increase in the C_D for the K_2 occurred between 15° and 25°, with a pronounced decline immediately thereafter. Two distinct types of frictional forces were identified: lift-induced drag, stemming from vortex formation, and parasitic drag, resulting from fluid viscosity. While the diminution of parasitic drag was observable in the other models, it was less apparent in the K_2. This situation suggests that the K2's design might benefit from modifications that specifically address its parasitic drag characteristics. This anomaly can be ascribed to the generation of low-pressure zones between the roughness structures on the K2's upper surface at a 22° αoα.
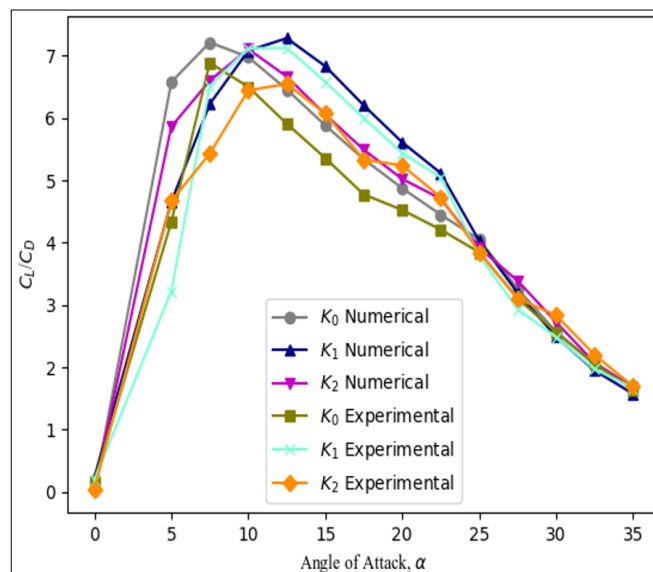

Figure 13. Comparison of C_L / C_D values of K_0, K_1 and K_2 models.

In Fig. 13, the C_L/C_D for the K_0, K_1, and K_2 across the 0-35° αoα range were scrutinized. Within this framework, an expeditious enhancement in C_L/C_D was discerned for all three models from 0 to 5°. In the experimental analysis, it was observed that the K_0, K_1, and K_2 attained their peak C_L/C_D values at 7.5°, 12.5°, and 12.5°, respectively. Upon reaching their apogee of C_L/C_D, it was noted that the K_1 model's value surpassed that of K_0 and K_2 by 2.85% and 8.5%, respectively. Subsequent to the models achieving their maximal αoα, a linear decrement in aerodynamic efficiency was observed, attributable to the swift escalation of C_D values. Between 10-25° αoα, the C_L/C_D of K_1 markedly outperformed the other two models, with the smooth blade exhibiting the lowest efficacy within these angular intervals. As previously elucidated in Fig. 12, K_1's superior performance within these αoα ranges compared to the other models is attributed to its significantly lower C_D values.

The average aerodynamic efficiency, denoted as $C_L/C_{D,avg}$, represents the quotient of C_L/C_D values spanning the 10 to 25° interval, wherein these values were assessed. Utilizing Eq. 3, numerical analysis calculated the comparative $C_L/C_{D,avg}$ of K_1 to be 11% and 8% higher than that of K_0 and K_2, respectively. Although the three models exhibited proximate values in the 25-35° range, K_2

demonstrated marginally superior performance. An overarching analysis of Fig. 13 revealed that the roughness structure exerts a beneficial impact on both the maximal and $C_L/C_{D,avg}$.
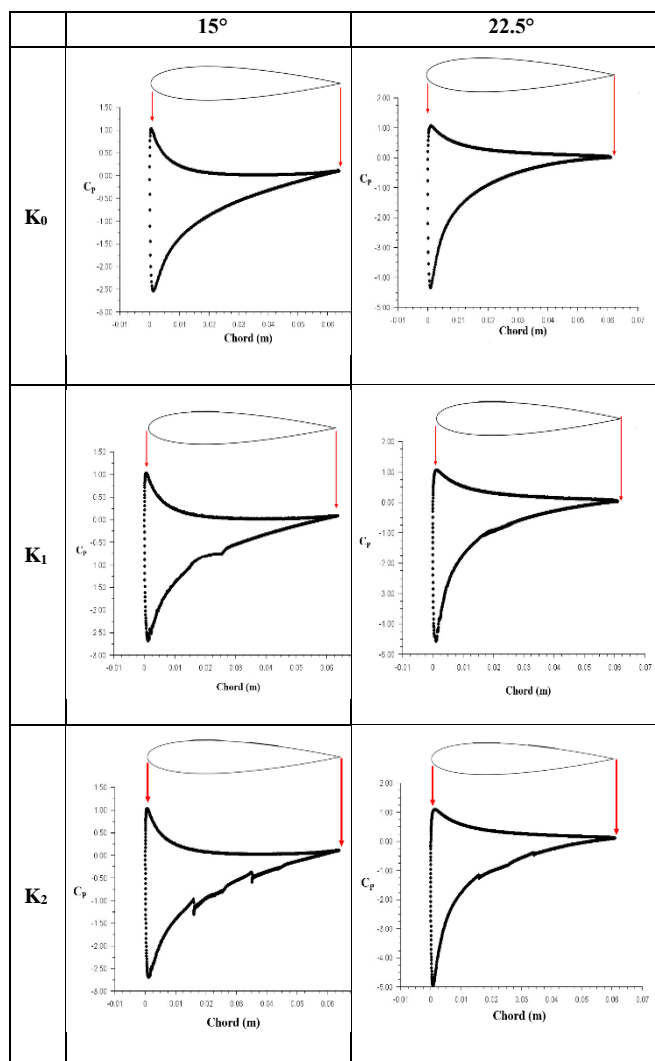

Figure 14. C_P for three turbine blade profiles at 15° and 22,5° αoα.

Fig. 14 illustrates the pressure coefficient (C_P) across the c of the K_0, K_1, and K_2 at both 15° and 22.5° αoα. For all blade models, a pronounced pressure differential was evident in the leading-edge region at both αoα. At 15°, a substantial pressure disparity spanned from the leading edge to the trailing edge on the upper surface of the blades, whereas at 22.5°, the magnitude of this pressure variation was significantly reduced. This reduction in pressure disparity at 22.5° facilitated the emergence of turbulence in the upper region of the blade surfaces, attributable to vortex generation. Consequently, the pressure attained a distinctively lower minimum level, as the flow was not sustained over a considerable portion of the blade surface. Upon meticulous examination of the K_2, it was discerned that the C_P in the vicinity of the roughness structure's commencement exhibited a disparate acceleration in comparison to the K_0. The roughness structure engendered lower pressure zones within this blade region, thereby enhancing the generation of a higher C_L.

In Fig. 15, the pressure contours and streamline configurations for the K_0, K_1, and K_2 at 15°, 22.5°, and 35° are depicted. In the K_0 model, a linear increase in vortex formation from the trailing edge towards the leading edge is

noted, attributable to the escalation in the αoα. This pattern of vortex formation is a key indicator of how the blade surfaces interact with the flow field, particularly in terms of energy transfer and boundary layer behavior. Conversely, in the K_1 and K_2 models, vortex zones are identified in vicinities where the roughness structures terminate. While the upper surface of the flat airfoil model predominantly exhibits laminar flow, the introduction of roughness structures in the K_1 and K_2 culminates in regions of heightened turbulence.
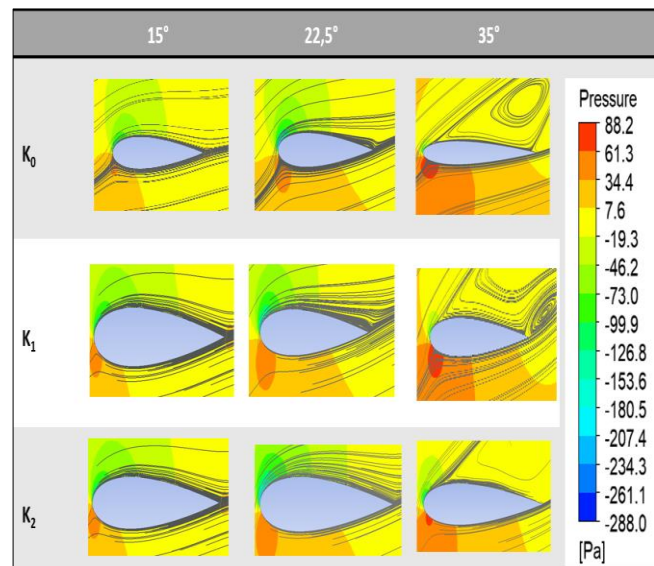

Figure 15. Pressure contours and streamlines of blade profiles at 15 °, 22.5 ° and 35 °, respectively a) K_0 b) K_1 and, c) K_2.
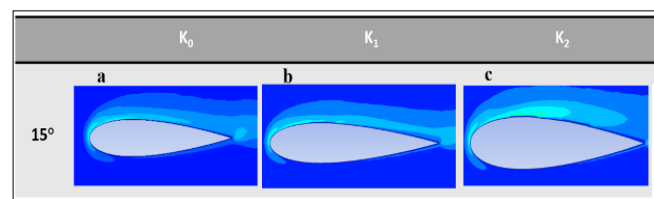

Figure 16. Turbulence kinetic energy of blade profiles at 15°, 22.5° and 35°, respectively a) K_0 b) K_1 and, c) K_2.

Fig. 16 presents the turbulence kinetic energy distribution profiles for K_0, K_1, and K_2 at a 15° αoα. Flow separation on the blade surface engenders turbulence, with turbulence kinetic energy serving as a pivotal indicator of the initiation point, magnitude, and directional trajectory of the turbulent zone. For the K_0, an intensification of turbulence kinetic energy is observed as the flow progresses towards the trailing edge at a 15° αoα. However, in the K_1 and K_2 models, wake regions emerge at both the mid and trailing edges of the turbine blade profiles, a consequence of the roughness surfaces. The emergence of these wake regions is a direct result of how the roughness modifies the flow, emphasizing the importance of surface roughness in controlling flow separation. As unequivocally demonstrated in Fig. 16c, the K_2 model exhibits a substantially higher turbulence density on the upper side of the blade relative to the other models, aligning with the C_L & αoα graph in Fig. 11, where the K_2 is attributed with the peak C_L value at 15°.

In summation, while the K_0 reveals turbulence intensity propagation from the trailing edge towards the leading edge across its surface pre-stall, the K_1 and K_2 not only exhibit turbulence density migration from the trailing to the leading edge but also within and between the roughness structures at

the blade's posterior regions. This configuration results in superior C_L/C_D for the K_1 and K_2 in the pre-stall phase. Post-stall, however, the aerodynamic efficiency contributions of the roughness structures are observed to be constrained.

The results of this study demonstrate that the effects of rough surfaces on aerodynamic performance extend beyond simply enhancing flow attachment. They also offer a deep understanding of how these effects can alter the aerodynamic characteristics of a airfoil, particularly the stall angle. These findings provide significant insights into how the use of rough surfaces in aerodynamic design can be optimized not just for maximizing the aerodynamic advantages of a specific surface but also for improving the overall aerodynamic performance of the airfoil. In this study, the positive effects of surface roughness on aerodynamic performance have been substantiated, particularly through its influence on the coefficient of pressure.

5. Conclusion

In this investigation, NACA 0015 turbine blade profiles with varying rough surfaces, alongside a smooth surface, were scrutinized for their aerodynamic performance, encompassing the lift-to-drag ratio (C_L/C_D), lift coefficient (C_L), drag coefficient (C_D), and turbulence kinetic energy. The gathered data from this study, incorporating both numerical outcomes from Ansys Fluent and experimental findings, were juxtaposed for analysis. The ensuing conclusions can be drawn from this investigation:

- The amalgamation of experimental and numerical analyses substantiates that the implementation of passive flow control methodologies exerts a favorable influence on the aerodynamic efficiency of the airfoil.
- CFD analyses employing diverse turbulence models revealed closely aligned results at lower αoα, with disparities emerging due to increases in αoα. This variation stems from the flow's transition to irregularity, where different turbulence models offer divergent approaches to resolving the phenomenon.
- The onset of stall was pinpointed at a 25° αoα for the K_0 within the analytical framework. Additionally, stalls were precipitated at a 22.5° αoα for the K_1 and K_2. A congruence in stall angle values was observed when experimental studies were aligned with analytical results.
- In the experimental analysis, relative to the maximal C_L values, the K_2 profile exhibited a 21% and 19% enhancement over the K_0 and K_1 profiles, respectively. Post-stall, the K_2 demonstrated a notably higher C_L performance compared to the other models, as confirmed through experimental and numerical methods.
- Between 10-25° αoα, K_1 showed a more advantageous C_D performance than both K_0 and K_2, a finding substantiated by numerical analysis, particularly at higher αoα. At the stall angle of 22.5°, it has been established that the C_D value for K_2 exceeds those of K_1 and K_0 by 10.41% and 38.46%, respectively.
- The peak C_L/C_D values were recorded at αoα of 7.5° for K_0, 12.5° for K_1, and 12.5° for K_2, with K_1 showing 2.85% and 8.5% higher optimal C_L/C_D ratios than K_0 and K_2, respectively, as determined through numerical analysis.
- According to numerical analysis, the $C_L/C_{D,avg}$ for K_1 was found to be 11% and 8% higher than that of K_0 across all αoα, highlighting K_1's enhanced aerodynamic efficiency through the use of numerical methods.

The results of this study demonstrate that the effects of rough surfaces on aerodynamic performance extend beyond simply enhancing flow attachment. They also offer a deep understanding of how these effects can alter the aerodynamic characteristics of a airfoil, particularly the stall angle. These findings provide significant insights into how the use of rough surfaces in aerodynamic design can be optimized not just for maximizing the aerodynamic advantages of a specific surface but also for improving the overall aerodynamic performance of the airfoil.

Author contribution statements

In the scope of this study, Himmet Erdi TANÜRÜN has made contribution to the concepts of literature review, research planning, design and direction of experimental studies, evaluation of results, supply of resources and materials, and writing of the article.

In the scope of this study, Ahmet Giray AKIN has made contribution to the concepts of literature review, research planning, design and direction of experimental studies, supply of resources and materials, and writing of the article.

In the scope of this study, Adem ACIR has made contribution to design and direction of experimental studies, research planning, and evaluation of results.

In the scope of this study, İzzet ŞAHİN has made contribution to control of spelling, creation of graphics and tables from the results of experiments and writing of the article.

Nomenclature

AR	Aspect Ratio	-
C_l	Lift Coefficient	-
C_d	Drag Coefficient	-
C_l/C_d	Aerodynamic Efficiency	-
Re	Reynolds Numbers	-
C_P	Pressure Coefficient	-
$C_L/C_{D,avg}$	Average Aerodynamic Efficiency	-
c	Chord Length	m
V_∞	Free-Stream Velocity	m/sn
y^+	Thickness of Boundary Layers	m
y	The Distance of the Wall	m
k	Turbulence Kinetic Energy	m^2/s^2
A	Surface Area	m^2
R_a	Surface Roughness Magnitude	μm

Greek Symbols

αoα	Angle of Attack	degree
ε	Energy Dissipation Rate	m^2/s^3
G_k	Turbulence kinetic energy due to the Velocity	m^2/s^2
G_b	Buoyancy Kinetic Energy due to the Velocity	m^2/s^2
σ_k and σ_ϵ	Turbulent Prandtl Numbers	-
υ	Local Kinematic Viscosity of the Fluid	m^2/s
k	Turbulence Kinetic Energy	m^2/s^2
U^*	Friction Velocity	m/sn

Abbreviations

K_0	Smooth Blade
K_1	Single Roughness Blade
K_2	Double Roughness Blade

References:

[1] A. Dağdeviren, E. Gedik, A. Keçebaş, H. K. Pazarlıoğlu, K. Arslan, A. I. Alsabery, "Effect of Al2O3–SiO2/Water Hybrid Nanofluid Filled in a Square Enclosure on the Natural Convective Heat Transfer Characteristics: A Numerical Study," *Journal of Nanofluids*, 11(5), 772-781, 2022, doi: 10.1166/jon.2022.1881.

[2] H. E. Tanürün, İ. Ata, M. E. Canli, A. Acir, " Farklı Açıklık Oranlarındaki NACA-0018 Rüzgâr Türbini Kanat Modeli Performansının Sayısal ve Deneysel İncelenmesi," *Politeknik Dergisi*, 23(2), 31-381, 2020 doi:10.2339/politeknik.500043.

[3] M. H. Mohamed, "Performance investigation of H-rotor Darrieus turbine with new airfoil shapes," *Energy*, 47(1), 522-530, 2012, doi: 10.1016/j.energy.2012.08.044.

[4] İ. Şahin, A. Acir, "Numerical and experimental investigations of lift and drag performances of NACA 0015 wind turbine airfoil," *International Journal of Materials, Mechanics and Manufacturing*, 3(1), 22-25, 2015.

[5] N. M. Triet, N. N. Viet, P. M. Thang, "Aerodynamic analysis of aircraft wing," *VNU Journal of Science: Mathematics-Physics*, 31(2), 68-75, 2015.

[6] R. I. Rubel, M. K. Uddin, M. Z. Islam, M. Rokunuzzaman, "Comparison of Aerodynamics Characteristics of NACA 0015 & NACA 4415," *International Journal of Research – Granthaalayah*, 5(11), 187-197, 2016, doi: 10.20944/preprints201610.0095.v1.

[7] A. Ramadan, K. Yousef, M. Said, M. H. Mohamed, "Shape optimization and experimental validation of a drag vertical axis wind turbine," *Energy*, 151, 839-853, 2018, doi: 10.1016/j.energy.2018.03.117.

[8] H. E. Tanürün, A. G. Akın, A. Acır, "Rüzgâr türbinlerinde kiriş yapısının performansa etkisinin sayısal olarak incelenmesi," *Politeknik Dergisi*, 24(3), 1219-1226, 2021. doi: 10.2339/politeknik.845804.

[9] R. Çakıroğlu, H. E. Tanürün, A. Acır, F. Üçgül, S. Olkun, "Optimization of NACA 4412 augmented with a gurney flap by using grey relational analysis," *Journal of the Brazilian Society of Mechanical Sciences and Engineering*, 45(3), 167, 2023. doi: 10.1007/s40430-023-04089-x.

[10] M. M. M. Saad, S. B. Mohd, M. F. Zulkafli, W. M. E. Shibani, "Numerical analysis for comparison of aerodynamic characteristics of six airfoils," *AIP Conference Proceedings*, 1831, 020004, 2017, doi: 10.1063/1.4981145.

[11] V. Shukla, A. K. Kaviti, "Performance evaluation of profile modifications on straight-bladed vertical axis wind turbine by energy and Spalart Allmaras models," *Energy*, 126, 766-795, 2017, doi: 10.1016/j.energy.2017.03.071.

[12] M. Karthick, S. M. Kumar, "Investigation of Aerodynamic Performances of NACA 0015 Wind Turbine Airfoil," *International Journal of Engineering Research*, 5(4), 327-331, 2016, doi: 10.17950/ijer/v5s4/425.

[13] R. I. Rubel, M. K. Uddin, M. Z. Islam, M. D. Rokunuzzaman, "Numerical and experimental investigation of aerodynamics characteristics of NACA 0015 aerofoil," *International Journal of Engineering Technologies*, 2(4), 132-141, 2016, doi: 10.19072/ijet.280499.

[14] A. Kabir, M. S. Chowdhury, M. J. Islam, M. Islam, "Numerical Assessment of the Backward Facing Step for NACA 0015 Airfoil using Computational Fluid Dynamics," *1st International Conference on Advances in Science, Engineering and Robotics Technology (ICASERT)*, Bangladesh, May. 3-5, 2019, doi: 10.1109/ICASERT.2019.8934501.

[15] L. W. Traub, "Aerodynamic impact of aspect ratio at low Reynolds number*," Journal of Aircraft*, 50(2), 626-634, 2013. doi: 10.2514/1.C031980.

[16] M. Mizoguchi, Y. Kajikawa, H. Itoh, "Aerodynamic characteristics of low-aspect-ratio wings with various aspect ratios in low Reynolds number flows," *Transactions of The Japan Society for Aeronautical and Space Sciences*, 59(2), 56-63, 2016, doi: 10.2322/tjsass.59.56.

[17] H. E. Tanürün, A. Acir, "Modifiye edilmiş NACA-0015 kanat yapısında tüberkül etkisinin sayısal analizi," *Politeknik Dergisi*, 22(1), 185-195, 2019, doi: 10.2339/politeknik.391800.

[18] M. T. Javaid, U. Sajjad, S. S. ul Hassan, S. Nasir, M. U. Shahid, A. Ali, S. Salamat, "Power enhancement of vertical axis wind turbine using optimum trapped vortex cavity," *Energy*, 278, 127808, 2023, doi: 10.1016/j.energy.2023.127808.

[19] H. E. Tanürün, "Improvement of vertical axis wind turbine performance by using the optimized adaptive flap by the Taguchi method," *Energy Sources, Part A: Recovery, Utilization, and Environmental Effects*, 46(1), 71-90, 2024, doi: 10.1080/15567036.2023.2279264.

[20] I. Hashem, M. H. Mohamed, "Aerodynamic performance enhancements of H-rotor Darrieus wind turbine," *Energy*, 142, 531-545, 2018, doi: 10.1016/j.energy.2017.10.036.

[21] H. E. Tanürün, A. Acır, "Investigation of the hydrogen production potential of the H-Darrieus turbines combined with various wind-lens," *International Journal of Hydrogen Energy*, 47(55), 23118-23138, 2022, doi: 10.1016/j.ijhydene.2022.04.196.

[22] K. Malik, M. Aldheeb, W. Asrar, S. Erwin, "Effects of bio-inspired surface roughness on a swept back tapered NACA 4412 wing," *Journal of Aerospace Technology and Management*, 11, 1719, 2015, doi: 10.5028/jatm.v11.1021.

[23] W. Chakroun, I. Al-Mesri, S. Al-Fahad, "Effect of surface roughness on the aerodynamic characteristics of a symmetrical airfoil," *Wind Engineering*, 28(5), 547-564, 2004, doi: 10.1260/0309524043028136.

[24] F. Salazar and A. Barrientos, "Surface roughness measurement on a wing aircraft by speckle correlation," *Sensors*, 13(9), 11772-11781, 2013, doi: 10.3390/s130911772.

[25] Q. Zhang, M. Goodro, P. M. Ligrani, R. Trindade, S. Sreekanth, "Influence of surface roughness on the aerodynamic losses of a turbine vane," *ASME J. Turbomach*, 128, 568–578, 2006, doi: 10.1115/1.2175163.

[26] Y. Wang, H. Tong, H. Sima, J. Wang, J. Sun, D. Huang, "Experimental study on aerodynamic performance of deformable blade for vertical axis wind turbine," *Energy*, 181, 187-201, 2019, doi: 10.1016/j.energy.2019.03.181.

[27] M. E. Abdel-Latief, K. Elsayed, M. Madbouli Abdelrahman, "Aerodynamic study of the corrugated airfoil at ultra-low Reynolds number," *Advances in Mechanical Engineering*, 11(10), 1-15, 2019, doi: 10.1177/1687814019884164.

[28] J. T. Murphy and H. Hu, "An experimental study of a bio-inspired corrugated airfoil for micro air vehicle applications," *Experiments in fluids*, 49(2), 531-546, 2010, doi: 10.1007/s00348-010-0826-z.

[29] M. Tamai, Z. Wang, G. Rajagopalan, H. Hu, G. He, "Aerodynamic performance of a corrugated dragonfly airfoil compared with smooth airfoils at low Reynolds numbers*," 45th AIAA aerospace sciences meeting and exhibi*t, Jan. 8-11 2007, Reno, USA, doi: 10.2514/6.2007-483.

[30] Q. Zhang and P. M. Ligrani, "Wake turbulence structure downstream of a cambered airfoil in transonic flow: effects of surface roughness and freestream turbulence intensity," *International Journal of Rotating Machinery*, 8, 1-12, 2006, doi: 10.1155/IJRM/2006/60234.

[31] Y. Xia, O. Bilgen, M. I. Friswell, "The effect of corrugated skins on aerodynamic performance," *Journal of Intelligent Material Systems and Structures*, 25(7), 786-794, 2014, doi: 10.1177/1045389X14521874

[32] Liu, Y., Zhang, K., Tian, W., Hu, H., "An experimental study to characterize the effects of initial ice roughness on the wind-driven water runback over an airfoil surface," *International Journal of Multiphase Flow*, 126, 103254, 2020, doi: 10.1016/j.ijmultiphaseflow.2020.103254

[33] Sun, Z., Mao, Y., Fan, M., "Performance optimization and investigation of flow phenomena on tidal turbine blade airfoil considering cavitation and roughness," *Applied Ocean Research*, 106, 102463, 2021, doi: 10.1016/j.apor.2020.102463

[34] M. Wang, C. Yang, Z. Li, S. Zhao, Y. Zhang, X. Lu, "Effects of surface roughness on the aerodynamic performance of a high subsonic compressor airfoil at low Reynolds number," *Chinese Journal of Aeronautics*, 34(3), 71-81, 2021, doi: 10.1016/j.cja.2020.08.020.

[35] M. Özkan, O. Erkan, "Control of a boundary layer over a wind turbine blade using distributed passive roughness," *Renewable Energy*, 184, 421-429, 2022, doi: 10.1016/j.renene.2021.11.082.

[36] J. Kelly, C. Vogel, R. Willden, "Impact and mitigation of blade surface roughness effects on wind turbine performance," *Wind Energy*, 25(4), 660-677, 2022, doi: 10.1002/we.2691.

[37] Y. D. Dwivedi, A. Wahab, A. D. Pallay, A. Shesham, "Effect of surface roughness on aerodynamic performance of the wing with NACA 4412 airfoil at Reynolds number 1.7×10^5," *Materials Today: Proceedings*, 56, 468-476, 2022, doi: 10.1016/j.matpr.2022.02.153.

[38] J. Ryi, W. Rhee, U. C. Hwang, J. S. Choi, "Blockage effect correction for a scaled wind turbine rotor by using wind tunnel test data," *Renewable Energy*, 79, 227-235, 2015, doi: 10.1016/j.renene.2014.11.057.

[39] A. Tools, "NACA 4-digit airfoil generator," National Advisory Committee for Aeronautics, 2015. http://airfoiltools.com/airfoil/naca4digit (accessed July. 11, 2024).

[40] J. Yao, W. Yuan, J. Xie, H. Zhou, M. Peng, Y. Sun, "Numerical simulation of aerodynamic performance for two dimensional wind turbine airfoils," *Procedia Engineering*, 31, 80-86, 2012, doi: 10.1016/j.proeng.2012.01.994.

[41] S. J. Kline, F. A. McClintock, Describing uncertainties in single-sample experiments, *Mechanical Engineering* 75, 3–8, 1953.

[42] J. Anderson, Computational Fluid Dynamics: The Basics with Applications. McGraw-Hill Education, 1995.",

[43] H. E. Tanürün, "Taguchi Yöntemiyle Sağlamlık Oranının Dikey Eksenli Rüzgâr Türbini Performansına Olan Etkisinin Sayısal Olarak İncelenmesi*," Journal of Materials and Mechatronics: A*, 4(2), 355-372, 2023, doi: 10.55546/jmm.1295748.

[44] M. Tahani, N. Babayan, S. Mehrnia, M. Shadmehri, "A novel heuristic method for optimization of straight blade vertical axis wind turbine," *Energy Conversion and Management,* 127, 461-476, 2016, doi: 10.1016/j.enconman.2016.08.094.

[45] H. F. Lam, H. Y. Peng, "Study of wake characteristics of a vertical axis wind turbine by two-and three-dimensional computational fluid dynamics simulations," *Renewable Energy*, 90, 386-398, 2016, doi: 10.1016/j.renene.2016.01.011.

[46] R. H. Rogers, Fluid Mechanics. Tata McGraw Hill Education Private, 1978.",

[47] M. H. Mohamed, A. M. Ali, A. A. Hafiz, "CFD analysis for H-rotor Darrieus turbine as a low speed wind energy converter," *Engineering Science and Technology, an International Journal*, 18(1), 1-13, 2015, doi: 10.1016/j.jestch.2014.08.002.

[48] A. F. Kaya, H. E. Tanürün, A. Acır, "Numerical investigation of radius dependent solidity effect on H-type vertical axis wind turbines," *Politeknik Dergisi*, 25(3), 1007-1019, 2021, doi: 10.2339/politeknik.799767.